



This work was carried out in whole or in part within the framework of the NOMATEN Centre of Excellence, supported from the European Union Horizon 2020 research and innovation program (Grant Agreement No. 857470) and from the European Regional Development Fund via the Foundation for Polish Science International Research Agenda PLUS program (Grant No. MAB PLUS/2018/8), and the Ministry of Science and Higher Education's initiative "Support for the Activities of Centers of Excellence Established in Poland under the Horizon 2020 Program" (agreement no. MEiN/2023/DIR/3795).

The version of record of this article, first published in *Separation and Purification Technology*, Volume 351, 24 December 2024, 128074, is available online at Publisher's website: <https://doi.org/10.1016/j.seppur.2024.128074>

This manuscript version is made available under the CC-BY-NC-ND 4.0 license.

Evaluation of tetracycline photocatalytic degradation using NiFe₂O₄/CeO₂/GO nanocomposite for environmental remediation: In silico molecular docking, Antibacterial performance, degradation pathways, and DFT calculations

Misbah latif¹, Raziq Nawaz^{2,3}, Muhammad Hammad Aziz^{1,2,*}, Muhammad Asif¹, Fatima Noor¹, Amil Aligayev^{2,3,4}, Syed Mansoor Ali⁵, Manawwer Alam⁶, Stefanos Papanikolaou⁴, Qing Huang^{2,3,**}

¹Department of Physics, COMSATS University Islamabad, Lahore Campus, 54000, Lahore, Pakistan

²Institute of Intelligent Machines, Hefei Institutes of Physical Science, Chinese Academy of Sciences, Hefei 230031, China

³University of Science and Technology of China, Hefei, 230026, China

⁴NOMATEN Centre of Excellence, National Centre for Nuclear Research, 05-400 Swierk/Otwock, Poland

⁵Department of Physics and Astronomy, College of Science, P.O. BOX 2455, King Saud University, Riyadh 11451, Saudi Arabia

⁶Department of Chemistry, College of Science, P.O. BOX 2455, King Saud University, Riyadh 11451, Saudi Arabia

Corresponding Authors:

*Muhammad Hammad Aziz; hammadaziz@cuilahore.edu.pk

**Qing Huang: huangq@ipp.ac.cn

Abstract

Graphene-based nanostructures with distinct structural and physicochemical characteristics may be able to photodegrade antibiotics effectively. Herein, this study reports the successful synthesis of NiFe₂O₄/CeO₂/GO nanocomposite (NC) by anchoring NiFe₂O₄/CeO₂ to the surface of GO (Graphene oxide). All state-of-the-art characterization techniques investigated the nanostructure, crystallinity, phonon modes, chemical composition analysis, elemental composition, surface area, magnetic properties, and optical band gap. Hydrothermal approach assisted NiFe₂O₄/CeO₂/GO catalyst showed better charge carrier separation and prompted the tetracycline (TC-HCl) photocatalytic degradation under visible light. Following 90 minutes of exposure to visible light, NiFe₂O₄/CeO₂/GO nanocomposite demonstrated superior photocatalytic activity, with a TC-HCl degradation rate of 95%. Reasonable mechanisms of tetracycline degradation were proposed where the •OH and •O⁻ played a leading role based on identified intermediates. Moreover, tetracycline photodegradation intermediates and the optimal pathway were identified using LC-MS spectrometry. This study also performed Density Functional Theory (DFT) calculations for the prepared materials to validate the experimental data. In vitro, antibacterial studies were consistent with the molecular docking investigations of the NiFe₂O₄/CeO₂/GO nanocomposite against DNA gyrase and FabI from Escherichia coli (E. coli) and Staphylococcus aureus (S.

aureus). Lastly, the outcomes revealed a new potential for NiFe₂O₄/CeO₂/GO nanocomposite for improved photocatalytic performance, making it a promising photocatalyst for wastewater treatment.

Keywords:

Graphene Oxide; Tetracycline Hydrochloride (TC-HCl); Photocatalyst; Density Functional Theory (DFT); Photocatalysis; Antibacterial activity.

Introduction

Pharmaceuticals in aquatic ecosystems are mostly sourced via the constant discharge of wastewater from treatment plants, with additional sources including waste from agricultural areas, aquaculture activities, and cattle ranches [1, 2]. Pharmaceuticals are synthetic chemicals developed for clinical application as therapeutic medications. Because of how they are constructed, medicines can cause significant physiological changes in living organisms even when administered at very low doses. These substances, whether excreted as metabolites or unaltered, persist for long periods in the atmosphere as they are not physiologically destroyed or reduced [3, 4].

Antibiotic resistance genes (ARG) have been amassing as antibiotic usage has skyrocketed over the past few decades, posing a hazard to animal, plant, and human ecosystems [5-7]. The tetracycline antibiotic family is the second most extensively used class of pharmaceuticals globally [8, 9]. It is employed in various areas, including medicine, aquaculture, and animal husbandry. Tetracycline hydrochloride is often utilized to cure and avoid bacterial infections in rats, raptors, and amphibians [10]. Since urbanization and industry have expanded rapidly, there has been an overuse of TC-HCl antibiotics and poor management, which has led to more serious water pollution and poses a serious hazard to both humans and the environment. Due to its mutagenic and teratogenic effects, it has garnered much attention [11, 12]. In order to address the environmental problems associated with tetracycline, scientists have developed and implemented a number of approaches, including photocatalysis, adsorption, biological removal, and others. This has improved the water quality and capacity for self-purification that tetracycline has enabled. [13, 35 14]. Furthermore, magnetic ferrites-based photocatalyst has become an emerging candidate to decompose antibiotics in wastewater [15-17] due to its low cost, lack of secondary pollutants, and environment-friendly approach. As a result, the main goal is to develop a photocatalyst with excellent degrading performance for TC with efficient photo-generated carrier separation [18-21]. Significant interest has been shown in heterogeneous photocatalytic oxidation as a potentially effective technique for decomposing refractory environmental contaminants. Doping with transition metal ions [22] and combining them with other narrow-band gap semiconductors functioning as photocatalysts [23] have been the subjects of several recent investigations. Because of their suitable band gap, strong photocatalytic activity, and chemical stability, several additional materials, including CeO₂, SnO₂, ZrO₂, Sm₂O₃, Fe₂O₃, TiO₂, V₂O₅, WO₃, ZnO, CdS, Bi₂O₃, Sb₂O₃, Al₂O₃, and MoO₃, have been employed as conventional photocatalysts [24]. According to previous studies, a significant number of binary composites, like V₂O₅-TiO₂, V₂O₅-ZnO, Au/Fe₂O₃, and BiVO₄/FeVO₄, and an insignificant amount of ternary nanocomposites, like V₂O₅-WO₃/TiO₂, Ni/MgO-ZrO₂, and N-Fe₂O₃/FeVO₄ [25, 26], have been developed and synthesized for organic pollution under observations. Phenols are among the ecological contaminants that are largely excluded by semiconductor particles containing metal. Numerous studies indicate that cations such

as Fe^{3+} , V, Ni, Pt, Cr^{3+} , Cu^{2+} , Co, Au, Pd, or other ions might boost the photoactivity of nanoparticles [27].

Magnetic ferrites such as spinel ferrites have a structural formula MFe_2O_4 ($\text{M} = \text{Ag, Au, Mg, Mn, Co, Ni, Cu, and Ce}$). Magnetic ferrites are utilized in different applications including catalysis, drug delivery, magnetic resonance imaging (MRI), microwave devices, photocatalysis, and water treatment. Their structures and characteristics are mainly determined by the arrangement of the cations in the tetrahedral and octahedral displays. Due to their high chemical stability, magnetic ferrites have recently attracted the interest of numerous scientists. Currently, researchers have been interested in magnetic ferrite nanocomposites because of their exceptional chemical stability, excellent reusability, and also magnetically detached. Substantial research has been put into enhancing the structure of magnetic ferrite nanocomposite to address the key issues that prevent their effective use in wastewater treatment. Numerous studies have also demonstrated magnetic ferrite's potential for use in photocatalytic processes that are driven by visible light. Nickel ferrite is the most significant magnetic material among various ferrites due to its thermal stability, electromagnetic performance, chemical stability, and high Curie temperature [28-30]. The photocatalytic activity of nickel ferrite can be increased by incorporating the metal oxides nanoparticles such as ZnO , CeO_2 , MnO_2 , NiO , MgO , SnO_2 , CuO , and ZrO_2 , etc, which facilitate more effective separation of the photo-generated charge carriers when exposed to visible light [31]. Especially, Cerium oxide has received a lot of interest because of its wide bandgap ($E_g = 3.19 \text{ eV}$). Also, CeO_2 is a rare earth dioxide that is also used as a heterogeneous photo-catalyst and contains redox sequences between the Ce^{3+} (reduced) and Ce^{4+} (oxidized) oxidation states [32-34].

Graphene is considered a two-dimensional carbon network with sp^2 hybridization and is recognized due to its outstanding electrical properties, effective electron mobility, high surface area, and chemical stability [35]. Graphene's exceptional qualities can be leveraged by combining it with other nanomaterials to boost catalytic activities. By accepting photo-generated electrons and minimizing charge carrier recombination, graphene has the potential for very efficient catalytic destruction of contaminants. Graphene-related nanomaterials are also utilized to increase the catalytic activity because they have a higher absorption range and enhanced charge separation and transport [36]. Graphene-based nanocomposite acts as a better photocatalyst as reduces electron-hole recombination which boosts the electron transfer rate, and improves the adsorption of chemical species through π - π interactions. Liang et al. demonstrated the visible-light-active NiFe_2O_4 -rGO composite photocatalyst, which exhibited remarkable photocatalytic performance [37]. Deng et al. revealed that rGO/ SnS_2 / ZnFe_2O_4 enhanced the photocatalytic effectiveness by the presence of rGO [38]. The oxygenated moieties in GO create defects and functional sites, thereby influencing the material's electronic structure. Its high surface area provides an ideal platform for the interaction and stabilization of the composite components, ultimately influencing the electronic and catalytic properties of the NiFe_2O_4 / CeO_2 /GO system. To systematically elucidate these impacts, Density Functional Theory (DFT) computations were also performed in this study.

In this view, Ultimate research in the realm of photocatalysis technology includes developing and investigating high-performance materials that respond to sunlight. The widespread co-existence of harmful medicines and metal ions in wastewater makes the development of a multifunctional photocatalyst imperative for the high-efficiency treatment of these pollutants. Ion intercalation and

functionalization of the surface have been widely used to construct catalysts that include oxyanion modification into metal ferrites. The majority of oxyanions, such as CO_2^- and NO^- , may be intercalated directly in the metal ferrites catalysts' interlayer gaps. Furthermore, the thorough use of photocatalysis is severely limited by the quick pairing of photoelectron-hole pairs [39-41]. As a result, to solve this constraint, researchers have used a variety of approaches, such as morphological control, semiconductor composite, precious metal surface modification, and other ways, to change the metal oxides with another composite material [42-45]. Among them, it has been shown that the heterojunction and three-dimensional hierarchical frameworks greatly increase the utilization of light absorption and encourage carrier separation, which permits quick interfacial charge transfer and substantially upgrades the photoactivity. It is noteworthy that the majority of pertinent research focuses on organic pollutants, although in practice, wastewater treatment involves both organic materials and microbiological pathogens. Consequently, further thorough study is required to create a novel multifunctional degradation and disinfection catalyst based on ferrite nanocomposites that are linked to graphene [46,47].

Therefore, In this study, $NiFe_2O_4/CeO_2/GO$ nanocomposite was used to explore the photocatalytic performance of tetracycline. The findings demonstrated that $NiFe_2O_4/CeO_2/GO$ has greater stability and catalytic activity than $NiFe_2O_4/CeO_2$. Besides, the physical characteristics and physiochemical properties of $NiFe_2O_4/CeO_2/GO$ are characterized by state of art techniques. This investigation showed that the combination of $NiFe_2O_4/CeO_2$ and GO produced excellent photocatalytic activity, with rapid separation and quick transfer of photo-generated carriers. Photodegradation of TC-HCl into smaller molecular intermediates was investigated via LC-MS. In silico molecular docking simulations were conducted to investigate the potential bactericidal of the $NiFe_2O_4/CeO_2/GO$ nanocomposite against DNA gyrase and FabI from *E. coli* and *S. aureus*. Overall, this study offers an effective approach by using $NiFe_2O_4/CeO_2/GO$ as an excellent photocatalyst for wastewater treatment and industrial purposes as well.

2. Experimental procedure

2.1 Chemicals

Deionized (D.I) water, Tetracycline (TC-HCl), Nickel chloride Hexahydrate ($NiCl_2 \cdot 6H_2O$), Sodium Hydroxide (NaOH), Iron chloride Hexahydrate ($FeCl_2 \cdot 6H_2O$), Graphite, Cerium Nitrate ($Ce(NO_3)_3 \cdot 6H_2O$) were used in this research.

2.2 Synthesis of $NiFe_2O_4$, $NiFe_2O_4/CeO_2$ and $NiFe_2O_4/CeO_2/GO$ via hydrothermal approach

Nickel chloride Hexahydrate (3 g) and Iron chloride (6g) were dissolved in 500 mL DI water and agitated for 120 minutes. Afterward, NaOH (2g) was dissolved in 25 mL and further added drop by drop while constantly agitating the mixture. The resultant mixture was then subjected to heat at 180 °C for 6 hrs. in a stainless steel autoclave. After being separated, the solution was gently rinsed with DI water 5 times and then calcinated at 400°C for 6 hrs. Next, $NiFe_2O_4/CeO_2$ nanocomposite was synthesized via the hydrothermal method. Precursors such as 2 grams of ($NiCl_2 \cdot 6H_2O$), 4.5 grams of ($FeCl_2 \cdot 6H_2O$), and 2.5 grams of ($Ce(NO_3)_3 \cdot 6H_2O$) were mixed in D.I (750 mL) and agitated for 1 hr. The obtained mixture was stirred for a further 30 minutes while NaOH was mixed drop by drop again. After that, the obtained solution was then placed into a Teflon-lined autoclave

to go through the hydrothermal process at 200°C for 6 hrs. Later, the obtained powder was separated and thoroughly washed with D.I. water at least 5 times before calcinating for 12 hours at 500°C. GO was prepared by modifying Hummer's process [48]. Initially, 200 mg of graphene oxide was mixed in distilled water of 50 mL. Further, the GO solution was mixed with 100 mL of NiFe₂O₄/CeO₂ (1g) composite solution.

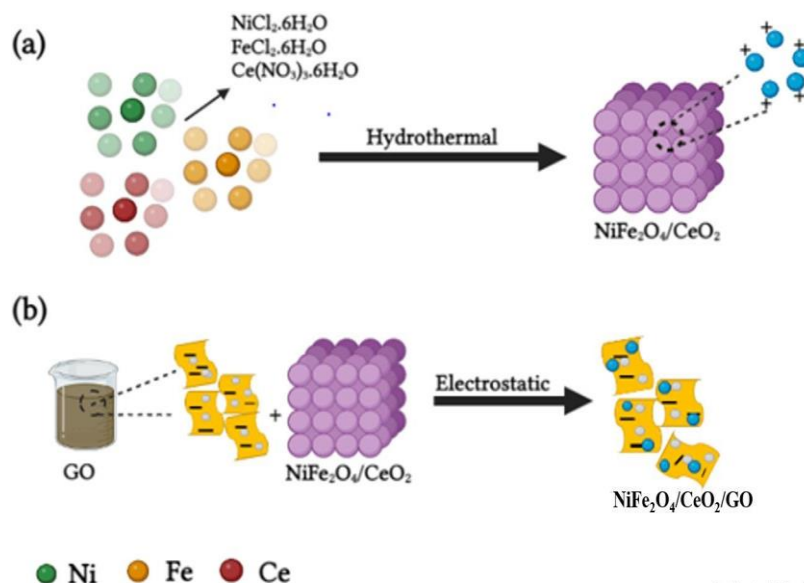


Figure 1: Schematic representation of NiFe₂O₄/CeO₂ and NiFe₂O₄/CeO₂/GO nanocomposite via hydrothermal process

The suspension was subsequently put through a 1-hour ultrasonication treatment at 60°C. Now, the solution was continuously stirred for 1 hour and further kept for 12 hours for aging. For hydrothermal treatment, the resulting solution was then subjected to a stainless steel autoclave at 180°C for 12 hrs. Lastly, the nanocomposite solution was centrifuged and calcinated at 400 °C for 4 hours to obtain the NiFe₂O₄/CeO₂/GO nanocomposite as illustrated in Figure 1.

2.3 Photocatalytic measurements

The photocatalytic activity was carried out at room temperature (25 °C) in quartz glass reactors. A 300 W Xe lamp with a 420 nm wavelength light source was used, and the surface was illuminated at a 50 W/m² intensity. Typically, photocatalyst (50 mg) was assorted to 100 mL of reaction fluid at 20 mg/L of tetracycline concentration in a reactor. The reaction mixture was agitated in the dark for about 30 minutes to achieve adsorption-desorption equilibrium. The suspension was filtered using 0.45 μm filters after being removed at regular intervals of 1 mL during irradiation. TC-HCl concentration was obtained by UV-Vis spectrophotometer in the collected solution while TC-HCl intermediates were evaluated using an LC-MS. A 250 mL mixture of DI water and 100 milligrams of NiFe₂O₄/CeO₂/GO catalyst was let to stand in the dark for half an hour. The resulting solution (3 mL) was taken at intervals of ten minutes, and they were stirred while being exposed to visible light. Under the specific protocols (pH level= 5, TC-HCl (20 mg/L), catalyst dose (1.5 g/L) & light exposure for 90 min). Nanocomposite catalytic properties were evaluated using pH (3.0, 5.0, 7.0, and 9.0) and co-existing anions (H₂PO⁻, Cl⁻, HCO²⁻, and 4 3 NO⁻) and optimized under simulated

visible light irradiation. IPA (2.0 mmol) for hydroxyl radicals, silver nitrate (2.0 mmol) for electrons, AO (2.0 mmol) for holes, and BQ (0.5 mmol) for superoxide anions were used as scavenging chemicals for trapping reactive radicals.

2.4 Recycling Experiments:

NiFe₂O₄/CeO₂/GO photocatalysts were recovered after the reaction was finished by filtering through polypropylene membranes and washing with acetone for five cycles while sonicated for five minutes. Following that, 5 mL of acetone was poured into the entire filtering membrane with the black cake on top in a beaker to produce a stable suspension that could be securely transferred to the storage vial. The sample was then dried using a vacuum. Following that, all of the chemicals and the solvent were added to the heterogeneous catalysts before starting a fresh catalytic cycle.

2.5 Antibacterial Activity:

NiFe₂O₄/CeO₂/GO antibacterial activity was evaluated against the bacterial strains that are commonly found in wastewater streams. The nanocomposite's bactericidal potential was investigated using the in-vitro disc diffusion method. The antibacterial efficacy of NiFe₂O₄/CeO₂/GO was examined against gram-positive *Staphylococcus aureus* (*S. aureus*) and gram-negative *Escherichia coli* (*E. coli*) bacterial strains. To prepare the glass petri plate for analysis, 20 mL of Muller Hinton agar coating was applied. Once the agar solidified, the designated type's 24-hour-old bacterial culture was swabbed onto the agar surface. NiFe₂O₄/CeO₂/GO combined circular discs (100 µg/disc) soaked in 10, 20, 30, and 40 µg/mL of the NiFe₂O₄/CeO₂/GO NC solution were facially added to this plate. chloramphenicol (3 µg/disc) was used as a positive control. The compounds were allowed to diffuse in the plates for 30 minutes, after which they were conditioned for 24 hours at 37 °C in an incubator. To determine the antibacterial activity of the NCs and controls, the clear zone of inhibition surrounding each disc was then assessed.

2.6 Molecular Docking Analysis

The molecular docking estimations of the NiFe₂O₄/CeO₂/GO nanocomposite focused on enzymes involved in nucleic acid and fatty acid biosynthesis pathways, which are considered promising targets for antibiotic development [49]. The AutoDock Vina software was utilized to perform molecular docking [50]. The 3D structural coordinates of the enzyme targets were obtained from the Protein Data Bank (PDB) with the following identification numbers: 5MMN for DNA gyrase [51], 1MFP [52], for enoyl-[acyl carrier protein] reductase (FabI) from *E. coli*, and 6TBC [53], for enoyl-[acyl carrier protein] reductase (FabI) from *S. aureus*. The analysis of the docked complexes and the 3D representation of binding patterns between the nanocomposite and active site residues were carried out using Discovery Studio, AutoDock Vina Visualizer, and PyMOL in conjunction [54]. Consistent with our earlier studies, 3D structures were analyzed using ChemSketch or SYBYL-X 2.0 to assess binding affinities with the active residues of particular proteins [55,56].

2.7 Characterizations

X-ray diffraction (XRD) was used to obtain the crystalline size via PANalytical X'Pert-PRO. Microstructures were investigated on FE-SEM (Hitachi; S-4500, Japan) while element analysis was explored via energy-dispersive X-ray spectroscopy (EDX) utilizing a 200 kV accelerating voltage. XPS analysis was determined on a photoelectron spectrometer (ESCALAB 250Xi). The chemical interaction of prepared materials was revealed by Fourier transform infrared (FTIR) spectroscopy. The Raman analysis was measured by a Raman spectrometer (Xplora Plus, France) to determine the Raman modes. After degassing the samples for 14 hours at 130 °C, the BET porosity was determined using the BELSORP MAX II instrument. The optical band gaps and absorption ranges of the prepared materials were attained via UV-Vis spectroscopy (Shimadzu, UV-2450, Japan). A vibrating sample magnetometer (Model-7410; Lake Shore; USA) was employed for the evaluation of the magnetization data. HPLC mass spectrometer (Agilent 1260 series, UK) was utilized to determine the TC-HCl intermediates produced during the photocatalytic activity. Electron spin resonance (ESR) was done on a spectrometer (Bruker ER200-SRC, Germany) to evaluate free radicals ($\bullet\text{OH}$, $\bullet\text{O}^-$).

3. Results and discussions

3.1 Characterization Techniques and Analysis

In Figure 2, XRD was used with a Cu-K α radiation source ($\lambda = 0.15402$ nm) to investigate the crystalline structure of NiFe₂O₄, NiFe₂O₄/CeO₂, and NiFe₂O₄/CeO₂/GO. XRD pattern for CeO₂ has the following distinctive planes (111), (200), (220), (311), (222), (400), (331), and (420) corresponds to 28.74°, 33.2°, 47.4°, 56.3°, 59.4°, 70.8°, 75.2° and 79.3° which recognized by a cubic fluorite structure as correspond to JCPDS No. 34-0394 and belongs to the space group Fm3m in Figure S1 [57, 58]. Moreover, Crystal planes of NiFe₂O₄ (111), (220), (311), (400), (422), (511), and (440) belong to 18.7°, 33°, 35.3°, 43.3°, 53.7°, 57.4°, 61.9° are interpreted to signify the cubic structure of NiFe₂O₄ as matched with JCPDS No. 86-2267 [59, 60]. Furthermore, XRD investigation of NiFe₂O₄/CeO₂ revealed the crystallinity as perceived in Figure 2. In NiFe₂O₄/CeO₂/GO nanocomposite, the diffraction peak of GO reveals at $2\theta = 10.2^\circ$ that is linked

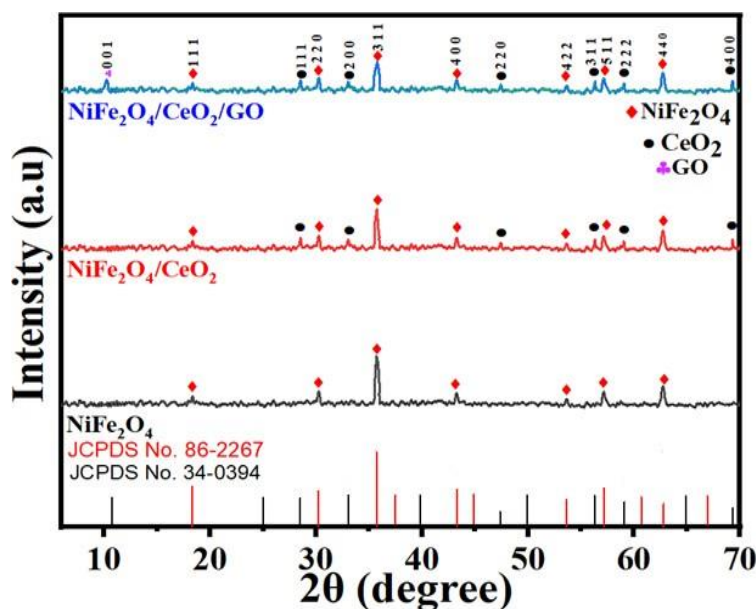


Figure 2: X-ray diffraction represents the crystalline structure of NiFe₂O₄, NiFe₂O₄/CeO₂, and NiFe₂O₄/CeO₂/GO nanocomposite to the interlayer space made possible by the oxygen functional group [61]. The Debye Scherrer's formula is used to determine the crystallite size of the prepared samples.

λ Signifies the wavelength of the X-ray beam, β shows the full-width half maximum (FWHM) and θ displays the Bragg's angle.

Figure 3 displays the morphological images from SEM of the prepared materials. In Fig. 3 (a), NiFe₂O₄ NPs were spherical, but the evident difference between nano-enabled NiFe₂O₄ and CeO₂ was visible. Moreover, NiFe₂O₄/CeO₂ exhibits some agglomeration processes as the metallic nanoparticles are easily agglomerated due to hydrophilic hydroxyl saturated residual bonds in different states on their surface as perceived in Figure 3 (b). Figure 3 (c) demonstrates the spherical nanoparticles of NiFe₂O₄/CeO₂ are arranged at the outermost layer wrinkles and GO interlayer structures. Additionally, NiFe₂O₄/CeO₂ has excellent dispersion and is well coated on the graphene oxide nanosheets, demonstrating the excellent performance of the hydrothermally synthesized NiFe₂O₄/CeO₂/GO nanocomposite [62]. The EDX spectrum of NiFe₂O₄, NiFe₂O₄/CeO₂, and NiFe₂O₄/CeO₂/GO nanocomposite are revealed in Figure 3 (d, e, & f). EDX analysis verified the high purity of the produced materials by confirming the presence of Ni, Ce, Fe, C, and O elements in the NiFe₂O₄/CeO₂ and NiFe₂O₄/CeO₂/GO nanocomposite and the FE-SEM and EDAX of CeO₂ in supplementary file Figure S2.

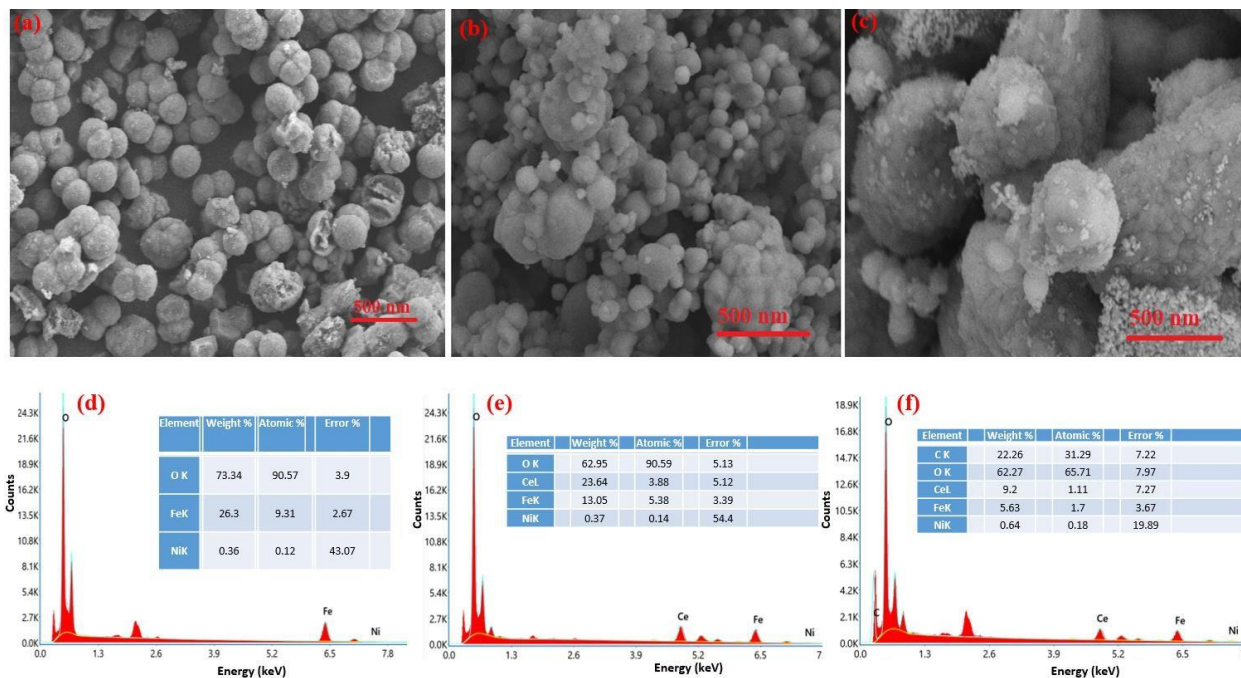


Figure 3: Morphological images of (a) NiFe₂O₄ (b) NiFe₂O₄/CeO₂ (c) NiFe₂O₄/CeO₂/GO exposed by FE-SEM and elemental composition revealed by EDAX of (d) NiFe₂O₄ (e)

NiFe₂O₄/CeO₂ (f) NiFe₂O₄/CeO₂/GO NC. Functional group analysis is represented by FTIR Spectroscopy as seen in Figure 4(a). The emergence of two major metal-oxygen bands between wavenumber 1000 cm⁻¹ and 400 cm⁻¹ provides evidence of ferrite's distinctive spinel structure. A prominent peak is shown in NiFe₂O₄ at 650 cm⁻¹ for the intrinsic tetrahedral metal-oxygen [Fe-O] vibrations (ν₁) and at 542 cm⁻¹ for the octahedral metal-oxygen [Ni-O] vibrations (ν₂). Based on the geometrical arrangement of the oxygen's closest neighbors, earlier reports indicate that the metal ions in ferrites are arranged in two distinct lattice sites, one tetrahedral and the other octahedral. The ferrite's vibrational spectra have a high frequency between 680-600 cm⁻¹, which resembles the inherent vibrational mode of tetrahedral, and a low frequency between 550-400 cm⁻¹, which corresponds to the octahedral site [63]. In the spectrum, (O-H) stretching vibration shows the high-frequency range at (3200-3600) cm⁻¹ and the less intense broadband at (1500-1550) cm⁻¹ for all prepared samples [64]. The band at 1315 cm⁻¹ causes C-O stretching vibrations for NiFe₂O₄ and NiFe₂O₄/CeO₂/GO, respectively [65]. It is generally known that for nanoparticles, the characteristic vibrational frequencies of a functional group will change if the surroundings of the group are even slightly changed. As grain size decreases, higher vibrational frequencies are observed [66]. In the NiFe₂O₄/CeO₂/GO spectra, the graphene oxide possesses functional groups like O-H, C-OH, COOH, and C-O.

The carboxyl O-H stretching mode is responsible for the GO's IR spectral peak between 3445cm⁻¹ and 2568cm⁻¹. The incorporation of alcohols with water molecules causes the O-H stretching absorption peak (3400 cm⁻¹) which is overlaid on the carboxylic acid's OH stretch to occur [67]. The asymmetric and symmetric CH₂ stretching of GO is responsible for peaks relating to 2968 cm⁻¹ and 2849 cm⁻¹, respectively [68]. Figure 4 (b) demonstrates the Raman analysis to identify structural flaws in carbon-based materials. In ferrites, spinel A and B-site ions contribute to the Raman modes such as Eg, A_{1g}, 3T_{2g}, A_{1g}, Eg, and T_{2g} are associated with octahedral and tetrahedral cations in NiFe₂O₄/CeO₂/GO nanocomposite [69]. Oxygen symmetries in tetrahedral AO₄ groups are responsible for peaks above 600 cm⁻¹. In NiFe₂O₄, the peak at 690 cm⁻¹ is attributed to A_g symmetry, while the peak around 320 cm⁻¹ signifies that E_g symmetry may be found in oxygen. Octahedral group vibrations are attributed to the frequencies of 470 and 570 cm⁻¹ for the F_{2g} mode. Ce-O (Fluorite structure, F_{2g}) symmetric stretching mode was perceived at 458 cm⁻¹ and 460 cm⁻¹, while defect induced oxygen vacancies mode at 596 cm⁻¹, and second order transverse acoustic (2TA) mode at (220 and 270 cm⁻¹) with the O-O stretching vibration for NiFe₂O₄/CeO₂ [70]. For NiFe₂O₄/CeO₂/GO, D and G peaks are identified from graphene at 1360 cm⁻¹ and 1595 cm⁻¹, respectively [71, 72]. However, Carbons with sp³ hybridization are presented by the D band, while sp² hybridization is revealed by the G band.

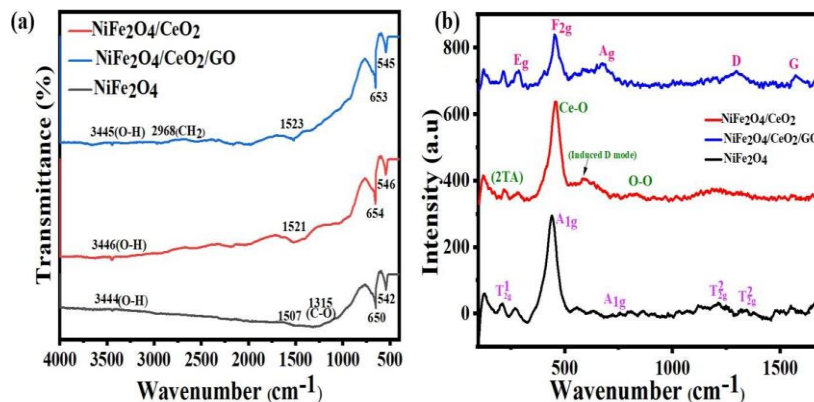


Figure 4: (a) FTIR Spectroscopy (b) Raman Spectroscopy of NiFe₂O₄, NiFe₂O₄/CeO₂, NiFe₂O₄/CeO₂/GO

In Figure 5 (a), Absorption spectra between 200 to 800 nm were assessed using UV-visible spectroscopy which represents the optical characteristics of the NiFe₂O₄/CeO₂, NiFe₂O₄, and NiFe₂O₄/CeO₂/GO NC [73] and the absorbance graph of CeO₂ in Supplementary file Figure S3. The occurrence of cations (Fe³⁺ & Ni²⁺) in the structure of the ferrite is indicated by a prominent absorbance peak in the visible area spectra between 250 and 700 nm [74]. It indicates that increased light absorption is useful to generate more electron-hole pairs, which may result in increased photocatalytic activity. Also, NiFe₂O₄/CeO₂ nanocomposite has a noteworthy absorption intensity in the visible range. In NiFe₂O₄/CeO₂/GO nanocomposite, the absorption spectrum displayed a peak corresponding (n → π*) transitions for (C=O) and (π → π*) transitions for aromatic (C-C) bonds which may occur due to the deoxygenation of the graphene oxide [75]. The band gap of synthesized materials was evaluated by the following formula [76].

$$(\alpha h\nu)^n = A(h\nu - E_g)$$

where α is absorbance constant, $h\nu$ indicates the energy of an incident photon, E_g represents band gap energy, Planck's constant (h), k has constant values. Plotting $(\alpha h\nu)^2$ vs $h\nu$ revealed the direct band gap of synthesized materials. Calculated 'E_g' values of CeO₂ (3.2 eV), NiFe₂O₄ (1.95 eV), NiFe₂O₄/CeO₂ (2.7 eV), and NiFe₂O₄/CeO₂/GO (2.68 eV) NC are shown in Figure 5 (b).

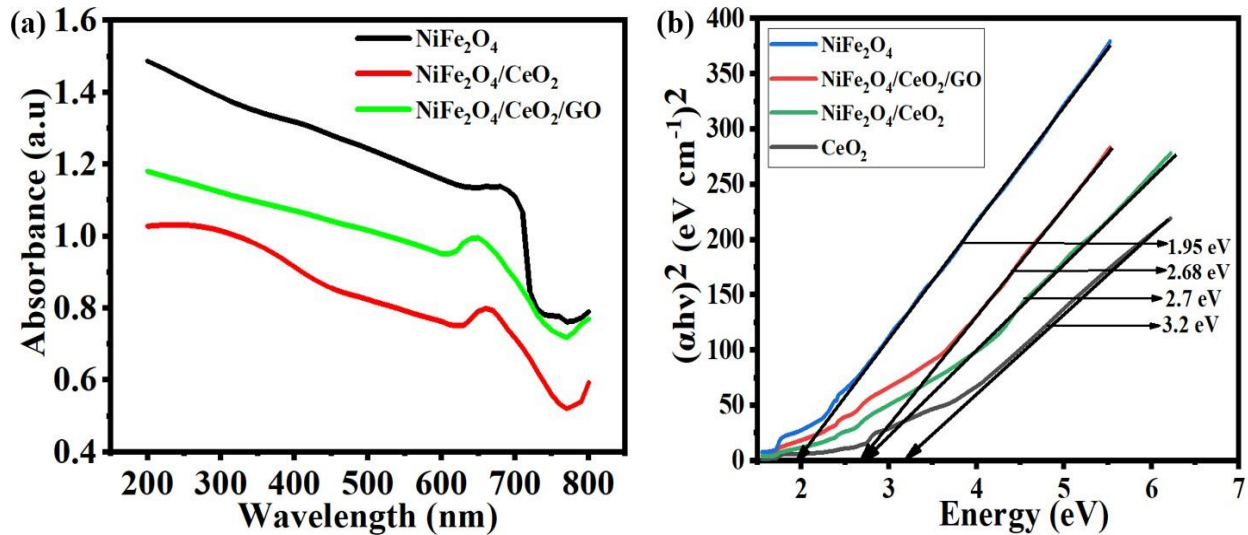


Figure 5: UV-visible Spectroscopy for NiFe₂O₄, NiFe₂O₄/CeO₂, and NiFe₂O₄/CeO₂/GO (a) Absorption spectra of (b) bandgaps calculated of all prepared materials via Tauc plot.

In Figure 6 (a), VSM examined the magnetic hysteresis curves of the NiFe₂O₄/CeO₂ and NiFe₂O₄/CeO₂/GO NC [77]. Shape, crystallinity, and the evolution of magnetization are all factors that contribute to the persistence of magnetic properties in magnetic materials [78]. At ambient temperature, the NiFe₂O₄/CeO₂ displays normal ferromagnetic activity, with a saturation magnetization (M_s) of around 34.79 emu/g [79]. NiFe₂O₄/CeO₂/GO nanocomposite has a

saturation magnetization (M_s) value of 12.21 emu/g. Since GO was added with $\text{NiFe}_2\text{O}_4/\text{CeO}_2$, therefore, it is expected that the magnetic component is substantially lower in GO, resulting in a lower total magnetization value. Coercivity and magnetization of $\text{NiFe}_2\text{O}_4/\text{CeO}_2$ are reduced when coated with GO, as the interaction between particles is reduced [80]. Magnetic parameters are calculated by the following equations as listed in Table S1.

The Brunauer Emmett Teller (BET) technique was used to estimate the specific surface area of each sample, and the Barret Joyner Halenda (BJH) method was used to calculate the mean diameter of the pores and total volume. The structural porosity of the samples was examined using these metrics. The nitrogen-gas adsorption /desorption isotherms' hysteresis loop is classified by the UPAC as illustrated in Figure 6 (b), and the associated inset BJH curves indicate the presence of mesoporous (2-25 nm) structure [81, 82]. Hysteresis loops, a feature of mesoporous structures, may be seen in the adsorption-desorption curves of all produced materials. The outcomes reveal that the specific surface area increases when GO is added, rising from 92 $\text{m}^2\cdot\text{g}^{-1}$ to a maximum of 160 $\text{m}^2\cdot\text{g}^{-1}$. The porous sheets of GO, a supporting layer, are responsible for the rise in the specific surface area. Nitrogen-gas adsorption /desorption isotherms' hysteresis loop of NiFe_2O_4 , $\text{NiFe}_2\text{O}_4/\text{CeO}_2$, and different surface area, pore volume, and pore sizes of all prepared samples are mentioned in supplementary Figure S4 and Table S2. To examine electrical conductivity and varied impedances, EIS was conducted between 0.1 Hz and 105 Hz in the frequency range. The comparable Nyquist curve of the electrode NiFe_2O_4 , $\text{NiFe}_2\text{O}_4/\text{CeO}_2$, and $\text{NiFe}_2\text{O}_4/\text{CeO}_2/\text{GO}$ EIS test is shown in Figure 6(c). The analogous series resistance (R_s) is displayed at the x-intercept. This resistance is made up of the junction resistance at the electrode material/substrate interface, the ionic resistance from the electrolyte, and the intrinsic resistance of the electrode material and substrate [83]. The lower R_s value of 1.1 Ω demonstrates highly appreciable electrical conductivity of the $\text{NiFe}_2\text{O}_4/\text{CeO}_2/\text{GO}$ electrode as compared to NiFe_2O_4 , $\text{NiFe}_2\text{O}_4/\text{CeO}_2$. The small diameter of the semi-circle implies a lower charge transfer resistance (R_{ct}) of 2.2 Ω . The high structural mesoporosity of $\text{NiFe}_2\text{O}_4/\text{CeO}_2/\text{GO}$ electrode materials shortens the charge transmission path across the electrode interface and KOH electrolyte solution [84,85].

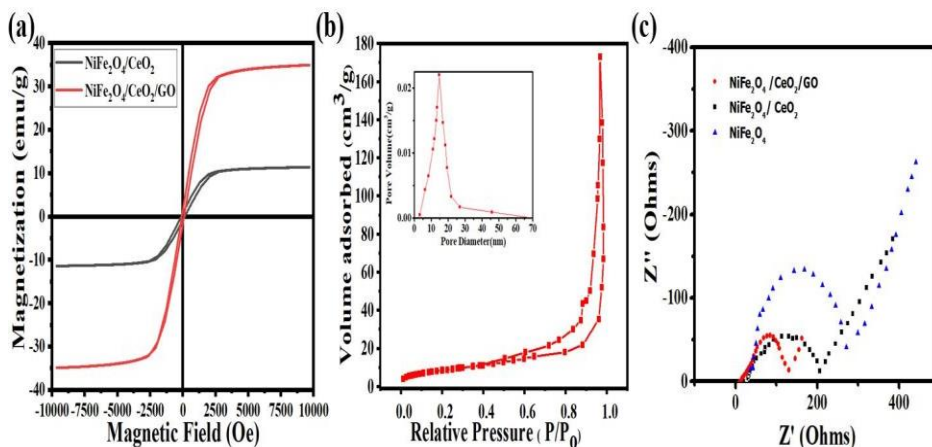


Figure 6: (a) Magnetization hysteresis behavior of NiFe_2O_4 and $\text{NiFe}_2\text{O}_4/\text{CeO}_2/\text{GO}$ NC (b) nitrogen-gas adsorption /desorption isotherms' hysteresis loop of $\text{NiFe}_2\text{O}_4/\text{CeO}_2/\text{GO}$ NC (c) EIS Nyquist plot of NiFe_2O_4 , $\text{NiFe}_2\text{O}_4/\text{CeO}_2$ and $\text{NiFe}_2\text{O}_4/\text{CeO}_2/\text{GO}$ NC

Fig. 7a clarifies the survey spectrum of (Ni, Ce, Fe, C, and O), which together make up the $\text{NiFe}_2\text{O}_4/\text{CeO}_2/\text{GO}$ NC. XPS study explains the existence of differential elements and metallic

species in NiFe₂O₄/CeO₂/GO composite. The Ni 2p_{3/2} and Ni 2p_{1/2} XPS spectra are shown in Fig. 7b. The primary peak of the Ni 2p_{3/2} spectrum is resolved into two distinct peaks located at 855.6 eV and 857.0 eV, respectively. These two peaks correspond to the valence states of Ni²⁺ and Ni³⁺, respectively. Furthermore, two satellite peaks are observed at energy levels of 863.3 eV and 880.3 eV. The locations of the deconvoluted and satellite peaks are in agreement with the values that have been reported [86]. In addition, the Ni 2p spectra exhibited two main peaks, namely Ni 2p_{1/2}, with signals centered at 872.5 eV, and 874.6 eV, which are indicative of Ni³⁺ and Ni²⁺ features, respectively [87]. Fig. 7c displays the Ce spectra of five distinct peaks with binding energies of 890.9 eV and 904.4 eV, which correspond to the Ce 3d_{5/2} and Ce 3d_{3/2} states, respectively. These states indicate the valence state of Ce³⁺. Furthermore, the peaks observed at the binding energies of 882.5 eV can be attributed to Ce 3d_{5/2}, whereas the peaks at 897.7 eV and 910.6 eV are associated with Ce 3d_{3/2}, indicating Ce⁴⁺ oxidation states [88]. Fig. 7d displays the core level Fe 2p_{3/2} spectra, which reveal two prominent peaks located at 710 eV and 724.5 eV. These peaks correspond to the valence states of Fe²⁺ and Fe³⁺, respectively, thereby verifying the successful functionalization of Fe₂O₄. The presence of Fe²⁺ and Ni³⁺ can be attributed to electron transfer between Ni and Fe ions (Fe³⁺ + Ni²⁺ ↔ Fe²⁺ + Ni³⁺). Similar findings have been reported for Co- Ti-doped M-type strontium hexaferrites [89]. The sp² hybrid C=C, sp³ hybrid C-C, and O-C=O of (C-1s) spectra peaks appear at (284.6, 287.47, and 288.5 eV) after deconvoluting the raw data to find overlapping peaks in Fig. 7e [90]. In Fig. 7f, numerous peaks in O-1s spectra that occur at (529, 531, and 532 eV) respectively, are attributed to oxygen, which exists in corresponding ester, hydroxyl, and carbonyl functional groups [91].

The primary peak at 530.7 eV represents the combination of lattice oxygen O²⁻ with Ni, Ce⁴⁺, and Fe²⁺. On the other hand, the peak at 533.2 eV refers to the presence of adsorbed oxygen in the catalyst. The oxygen that is adsorbed can produce free radical active species by trapping electrons that are created by light during the photocatalytic process. This helps to enhance the activity of the photocatalyst [92]. Therefore, according to Fig. 8b, NiFe₂O₄/CeO₂/GO nanocomposites exhibit superior adsorption performance compared to NiFe₂O₄ and NiFe₂O₄/CeO₂. This enhanced adsorption capability can contribute to the improvement of activity in the first stage of photocatalysis. Some of the Ce⁴⁺ in CeO₂ may catch electrons produced by light to form Ce³⁺. By incorporating Ce³⁺ into the NiFe₂O₄ structure, a new impurity level is created within the band gap, resulting in a reduction in the width of the band gap. Conversely, a heterojunction is created when CeO₂ and NiFe₂O₄ are combined, resulting in an expanded range of spectrum response and enhanced photocatalytic activity of the catalyst. The XPS figure (b,c&d) demonstrates that the photocatalytic efficiency of NiFe₂O₄/CeO₂ was enhanced when compared to CeO₂ and NiFe₂O₄. The combination of NiFe₂O₄ with CeO₂ forms a heterojunction, which enhances the separation of photo-generated electron-hole pairs and thus enhances the performance of composite photocatalyst materials [93]. The presence of graphene oxide (GO), which has high conductivity, enhances the movement of carriers at the interface and enhances the photocatalytic activity of the composite catalyst. Hence, NiFe₂O₄/CeO₂/GO exhibits superior adsorption and photocatalytic capabilities, resulting in a TC-HCl removal rate of 95 % after a 90-minute photoreaction.

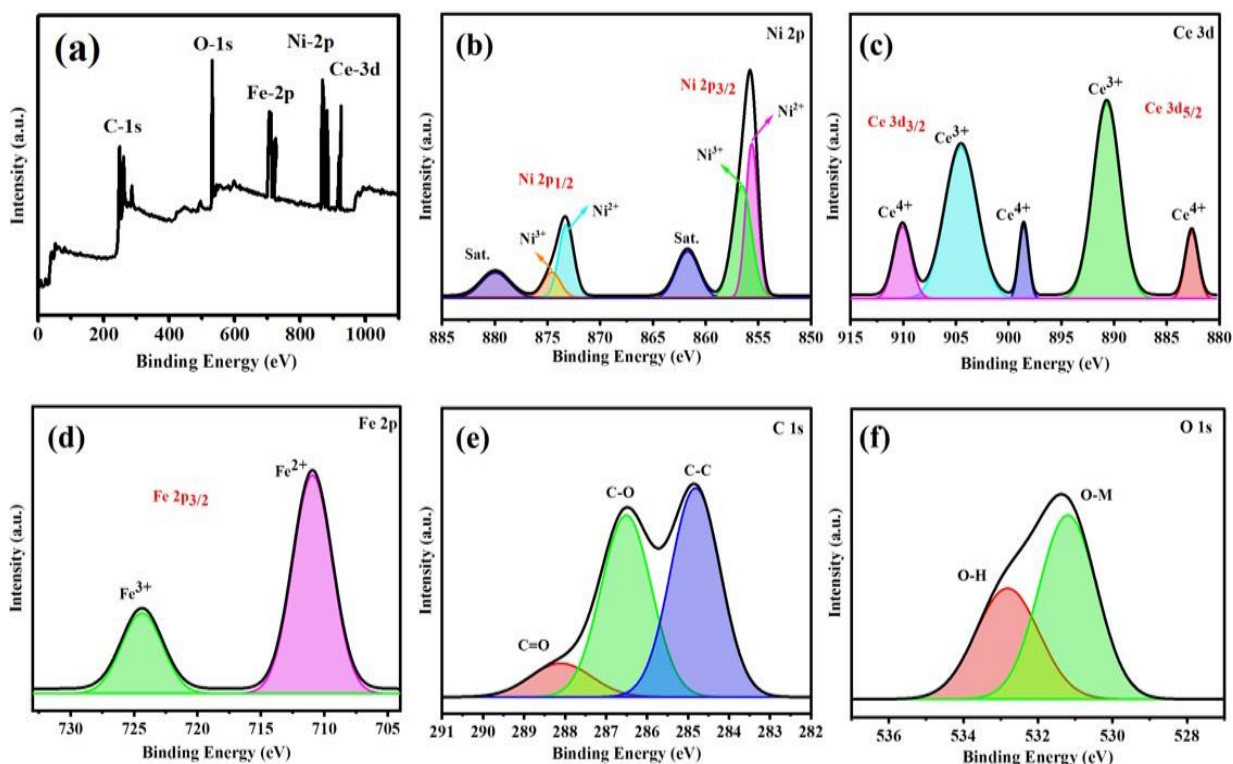


Figure 7: High-resolution XPS spectrum of NiFe₂O₄, NiFe₂O₄/CeO₂ and NiFe₂O₄/CeO₂/GO nanocomposite (a) complete spectrum (b) Ni 2p (c) Ce 3d (d) Fe 2p (e) O-1s (f) C-1s.

3.2 Photocatalytic performance, stability, and photodegradation of TC-HCl: A small amount of physical tetracycline-hydrochloride (TC-HCl) elimination by adsorption shows almost no effectiveness in the dark as shown in Figure 8 (a). Besides, following 90 minutes of visible light exposure, the degradation of TC-HCl in the photocatalyst's absence may also be ignored which indicates the photocatalysts and exposure to visible light are necessary for the degradation of tetracycline-hydrochloride. Alternatively, NiFe₂O₄/CeO₂/GO nanocomposite enhances the TC-HCl photodegradation performance to 95% as shown in Figure 8 (b). It is obvious that the interaction of NiFe₂O₄/CeO₂ with TC stimulates the production of numerous charge carriers when exposed to visible light and further by adding the GO, further suppresses electron-hole pair interaction. The improved photocatalytic efficacy of the nanocomposite catalysts has been related to a reduced rate of recombination between charge carriers and rapid transportation of photoinduced electron-hole couples. The following equation, which represents the pseudo-first-order kinetics model, is frequently used to demonstrate tetracycline degradation when exposed to photocatalysts.

$$-\ln (C/C_0) = kt$$

The rate constant (k) for photocatalytic degradation was determined using C and C₀ as starting and final concentrations. In Figure 8 (c&d), rate constant (k) was calculated to be 0.015 min⁻¹ for CeO₂, 0.019 min⁻¹ for NiFe₂O₄, 0.031 min⁻¹ for NiFe₂O₄/CeO₂, and 0.067 min⁻¹ for the nanocomposite of NiFe₂O₄/CeO₂/GO. The ability of nanocomposite materials to be recycled is essential in environmental remediation studies. The performance of the NiFe₂O₄/CeO₂/GO nanocomposite to degrade

tetracycline after five cycles of reusability is depicted in Figure 8 (e), and it shows that the catalyst retains its 95% photodegradation performance, demonstrating its superiority as a catalyst. The catalytic results provide evidence that photocatalysts may be employed in practical wastewater treatments [94].

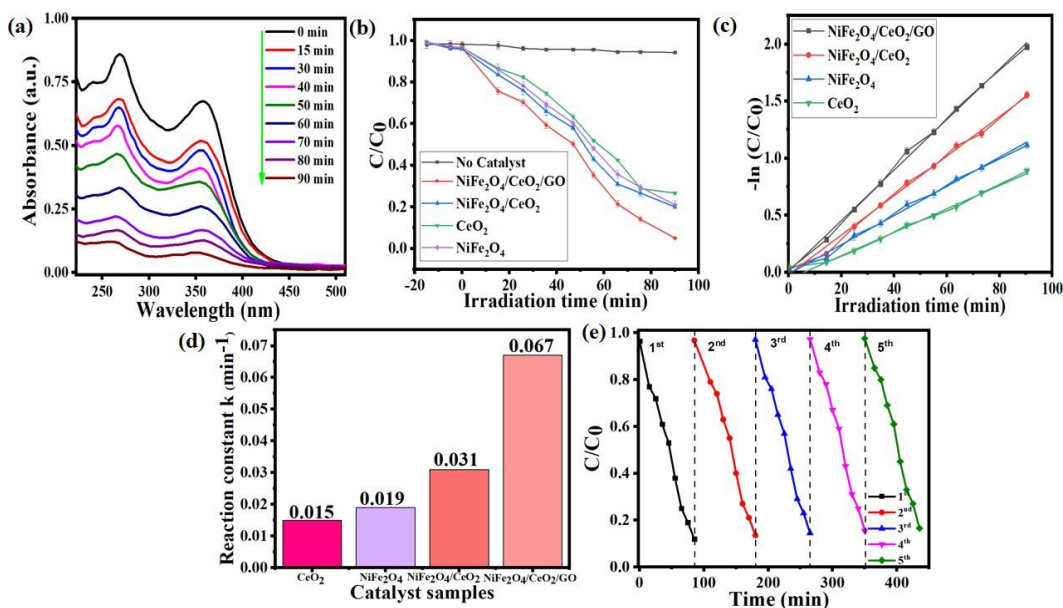


Figure 8: (a) variations in the tetracycline degradation show prominent absorbance at various times, (b) tetracycline Activity by using the prepared photocatalysts under visible light, (c) the kinetic plot using pseudo first order (d) all photocatalyst rate constant for TC-HCl (e) NiFe₂O₄/CeO₂ /GO photocatalyst stability investigation for TC-HCl degradation.

To ascertain the optimum starting TC-HCl concentration, the effectiveness of photocatalytic degradation was seen in Figure 9 (a) at TC-HCl concentrations between 10-50 mg/L. Figure 9 (a) shows the photocatalytic breakdown of TC-HCl to be reduced from 95% to 83% with an increase in the starting TC-HCl dose from 10 mg/L to 30 mg/L. It appears that the catalyst's catalytic performance is also influenced by the TC's initial concentration. However, when the TC dose was increased from 30 mg/L to 50 mg/L, it became apparent that the reason for the effectiveness of the degradation might be that the higher initial concentration of TC caused the NiFe₂O₄/CeO₂/GO active site to become saturated, resulting in less efficient degradation. [95]. During the TC-HCl photocatalytic process, pH may affect the stability of active species, the surface charge of catalysts, and the molecular structure of TC. The initial TC degradation efficiency was observed to decrease from 90% at pH 5 in Figure 9 (b). The outcomes showed that the maximum photocatalytic activity for TC breakdown was displayed by NiFe₂O₄/ CeO₂ /GO at pH=5.

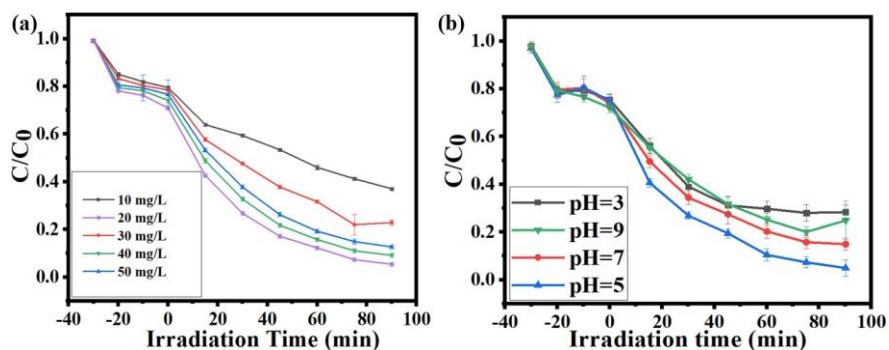


Figure 9: (a) TC-HCl curves analysis via different catalysts (b) photocatalysis Breakdown of TC-HCl for various pH ranges

Moreover, the impact of co-existing anions, such as $H_2PO_4^-$, Cl^- , NO_3^- and HCO_3^{2-} , on the degradation of TCH-Cl as mentioned in Figure S5. The co-existing anions hindered the photocatalytic degradation efficiencies, and the negative impact on TCH-Cl degradation declined in the following order: $HCO_3^- > H_2PO_4^- > Cl^- > NO_3^-$. The co-existing anions may function as free radical scavengers, decreasing the effects of dominant oxidizing radicals. Also, some anions may be adsorbed onto the NiFe₂O₄/CeO₂/GO photocatalyst's surface, lowering the degradation efficiency [96, 97, 98]. Also, TCH-Cl degradation efficiency is still greater than 88% when coexisting inorganic cations (such as Ca²⁺, Mg²⁺, or Na⁺) are present, as shown in Fig. S6. This suggests that the major metal cations do not inhibit the Photodegradation of TC-HCl via NiFe₂O₄/CeO₂/GO nanocomposite. The reaction solution for TC-HCl degradation using the NiFe₂O₄/CeO₂/GO nanocomposite was composed of three types of water matrices: pure water, tap water (Comsats University Islamabad, Lahore campus), and mineral water (Nestle) as seen in Figure S7. This was carried out to evaluate the impact of different water matrices for the practical usage of the photocatalyst in wastewater treatment. NiFe₂O₄/CeO₂/GO catalyst degraded TC-HCl with efficiencies of 92%, 89%, and 90% for pure water, tap water, and mineral water, respectively [99].

3.3 Scavengers Radical trapping and electron spin resonance:

In Figure 10 (a), the radical trapping tests on scavengers allowed for the identification of the numerous photogenerated species during TC-HCl breakdown. Ammonium oxalate (AO) and silver nitrate (AgNO₃) served as the scavengers for holes (h⁺) and electrons, while BQ and IPA performed as the scavengers for $\bullet O^-$ and $\bullet OH$ radicals. In Figure 10 (b), nearly 90% of TC was removed when there were no scavengers. BQ substantially slowed down the TC-HCl's ability to degrade, showing that superoxide anion radicals were the most active species in the breakdown of tetracycline hydrochloride. However, the addition of IPA and AgNO₃ showed a minimal effect on the TC-HCl photodegradation, indicating that hydroxyl radicals and electrons were also the significant reactive species for the tetracycline breakdown (degradation). In comparison, the presence of AO prevented the photocatalytic breakdown of TC-HCl, proving that holes were the primary active species [101]. The ESR procedure supports the emergence (generation) of photo-induced ($\bullet O^-$ and $\bullet OH$) radicals using DMPO serving as a trapping agent, as illustrated in Figure 10 (c & d) [102]. In both cases (DMPO $\bullet O^-$ and DMPO $\bullet OH$), ESR signals were evident within 5

and 10 minutes under the impact of visible irradiation, respectively while ESR signal was not noticed in the dark condition. Additionally, the signal strength increased by utilizing NiFe2O4/CeO2/GO and increasing the visible-light exposure to a duration of 10 minutes.

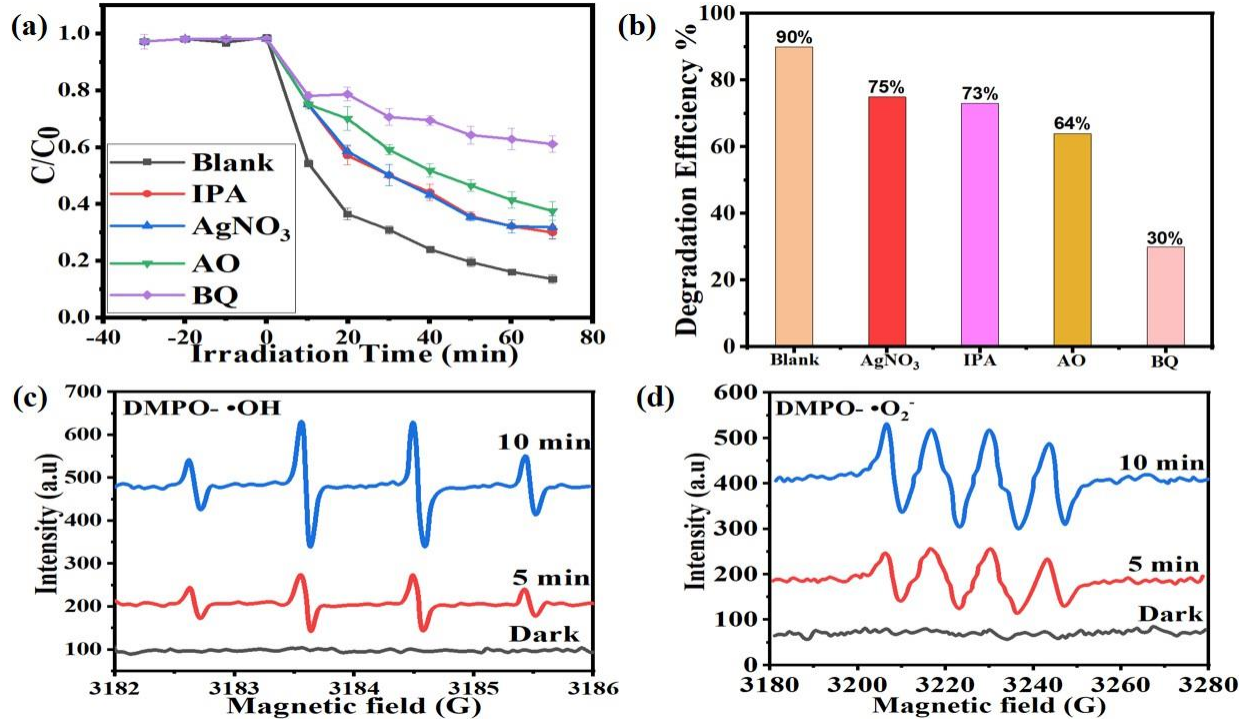


Figure 10: (a) Scavengers outcomes for TC-HCl breakdown degradation (b) Degradation efficiency of scavengers for tetracycline (c & d) ESR spectral signals for the hydroxyl and superoxide anions in both light and dark

Figure 11 displays the photocatalytic elimination of TC-HCl by the NiFe2O4/CeO2/GO nanocomposite. When NiFe2O4 and CeO2 nanoparticles are exposed to visible light, they cause the e^-/h^+ pair in the VB and CB, which is seen in the schematic diagram below in Figure 11. Therefore, the potentials of VB and CB were calculated by using the following equations [103].

$$E_{CB} = X - (E_{ef} + 0.5 E_g) \text{ \& } E_{VB} = E_{CB} + E_g$$

Where the valence band and conduction band potentials, respectively, are denoted by E_{CB} and E_{VB}. E_{ef} (free electron energy) which is equivalent to 4.5 eV on the hydrogen scale. The following equation may be used to compute E_g, which stands for the semiconductor's band gap energy, and X, which stands for the semiconductor's electronegativity:

$$X = [(A)^a \chi(B)^b \chi(C)^c]^{1/((a+b+c))}$$

where a, b, and c represent the number of atoms in each compound [104]. The band gap energy (E_g) and X of NiFe2O4 and CeO2 are 1.95 eV, 5.83 eV, and 3.2 eV, 5.56 eV, respectively. As a

result, NiFe₂O₄ and CeO₂ had ECB and EVB values of 0.36 eV, 2.31 eV, and -0.6 eV, 2.7 eV, respectively, compared to the NHE (Normal Hydrogen Electrode). Additionally, Figure 11 offers a clear illustration of the impact of graphene oxide nanosheets, that trap photoinduced electrons when transit from the VB to the CB. Superoxide radical anion ($\bullet O^-$) is produced when molecular oxygen is reduced during the electron transfer. However, hydroxyl radicals ($\bullet OH$) are created when valence band holes join with water molecules or hydroxyl groups to trigger oxidation. By reacting with tetracycline, these reactive species ($\bullet OH$, $\bullet O^-$) remove the color from the compound. The photocatalytic removal of tetracycline is illustrated by the following equations:

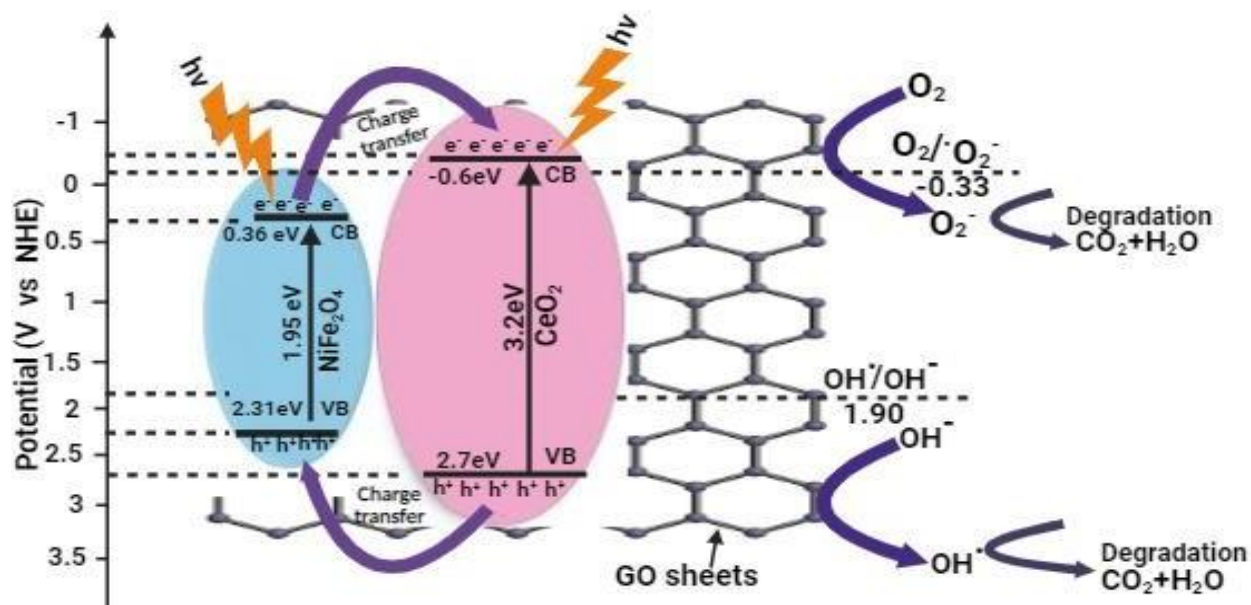
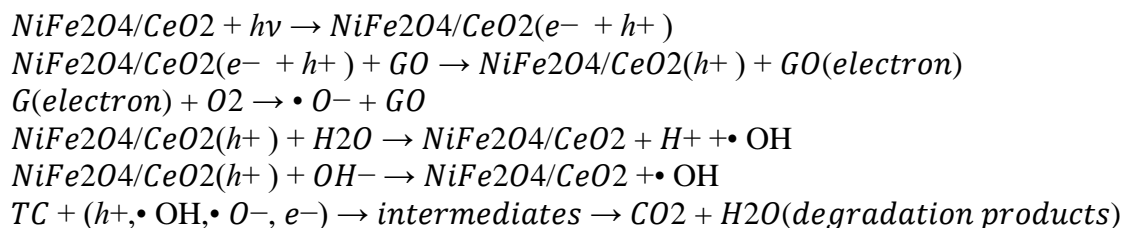


Figure 11: Schematic representation depicted the enhanced production of holes and superoxide anions during the photodegradation of tetracycline antibiotic using NiFe₂O₄/CeO₂/GO

The stability of the material in practical applications is also a significant aspect that must be considered into account when selecting the most effective photocatalyst [105]. Thus, the stability of the NiFe₂O₄/CeO₂/GO nanocomposite was assessed by the use of XRD and SEM measurements. As a result, the XRD pattern and SEM illustrations, which compare the phases and microstructure with those of the fresh one (Figure 12(a-c)), reveal the great stability of NiFe₂O₄/CeO₂/GO. The aforementioned results indicate that NiFe₂O₄/CeO₂/GO is a practicable material for wastewater treatment due to its large mineralization ability, superior stability, reusability, and high activity.

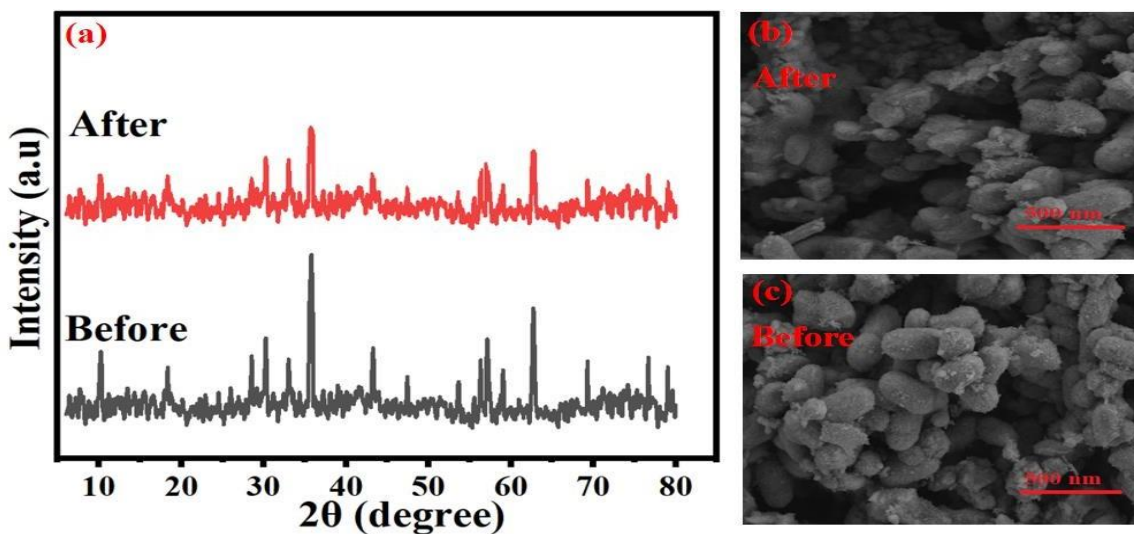


Figure 12: Stability analysis via (a) XRD and (b&c) SEM

3.4: Possible degradation pathways, intermediates, and toxicity assessment test:

Using an LC-MS system, the intermediates generated during the photocatalytic reaction were identified to get a better understanding of the NiFe₂O₄/CeO₂/GO nanocomposite-induced TC degradation process. Past studies have shown that TC decomposes readily due to the easy assault of active free radicals on electron-donating groups and ionizable groups (such as dimethylamino groups, amide groups, and double bonds) [106,107]. Three primary TC degrading mechanisms over NiFe₂O₄/CeO₂/GO are suggested in this work and shown in Figure 13. Since the C = C double bond in route 1 is very unstable and readily oxidized by •OH, the hydroxylation process results in P1 (m/z = 461) [108,109]. P4 (m/z = 338) is then produced as a result of the deamination and ring-opening reactions, while P7 (m/z = 307) is produced as a result of the subsequent de-hydroxylation process when h⁺, O⁻, and •OH are present [110]. Route 2: TC at m/z = 445 with SO^{•-} attack releases the -N(CH₃)₂ group, generating the P2 (m/z = 415) intermediate. Route 2 is another possibility. In this pathway, TC is subjected to dehydration, demethylation, and amino group loss, resulting in P5 (m/z = 318) and P8 (m/z = 246) [111,112]. Route 3 involves the easy assault of the amino group by h⁺ and •O⁻, which results in the creation of P3 (m/z = 429) through the deamination reaction and subsequent degradation into P6 (m/z = 399) through the demethylation process. Subsequently, a persistent oxidation process involving •O⁻ and •OH leads to a second degradation event that produces P9 (m/z = 302), in agreement with the earlier finding [113]. Finally, these intermediates are broken down and mineralized into tiny molecules by reactive species.

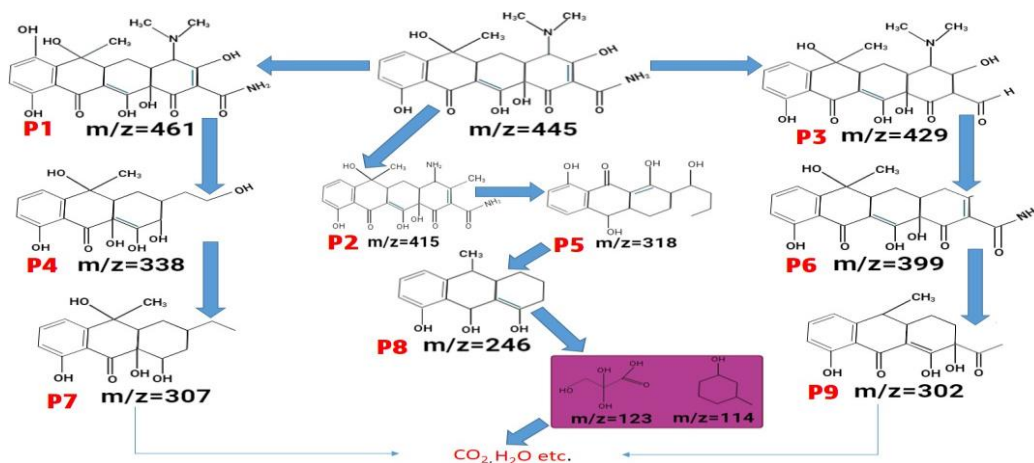


Figure 13: NiFe₂O₄/CeO₂/GO nanocomposite revealed the LC-MS pathway for the TC-HCl breakdown into smaller intermediate molecules

According to QSAR prediction, Toxicity Estimation Software (T.E.S.T.) was used to further assess the toxicity of TC and above intermediates that were converted from TC [114, 115]. Based on the findings, the majority of the intermediates had decreased in toxicity following the catalytic process. The fathead minnow's LC₅₀ for TC was 1 mg L⁻¹, as seen in Figure 14 (a), which is considered toxic. Even so, the LC₅₀ of fathead minnow for P-461, P-429, P-399, and P-338 was quite toxic, but the toxicity decreased to not be detrimental for the subsequent oxidation intermediates. The toxicity of TC for *Daphnia magna* rapidly declined, as seen in figure 14 (b) by the 48-hour LC₅₀ *Daphnia magna* of 10 mg L⁻¹, which was lower than that of nearly all the breakdown products. After development toxicity testing, it was found that half of the intermediates were less toxic to development than TC. In contrast, the other half was marginally more toxic to development than TC (Figure 14 (c)). According to the toxicity estimates above, the overall degradation process was low toxicity. It could deteriorate by raising the mineralization level and extending the reaction time, even while a tiny percentage of the intermediaries remained toxic. As a result, the combination demonstrates the ability of the NiFe₂O₄/CeO₂/GO nanocomposite oxidation system to break down and lessen TC toxicity efficiently.

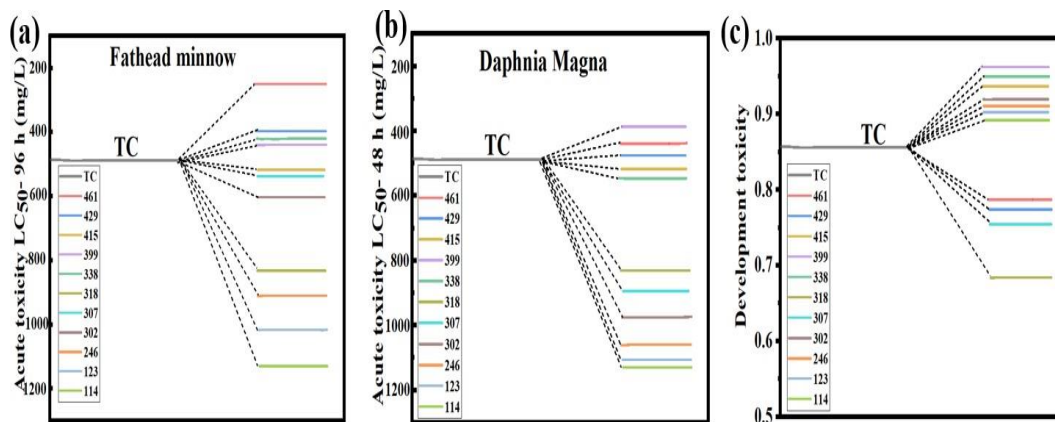


Figure 14: Acute toxicity for (a) Fathead minnow 96-h (b) *Daphnia Magna* 48-h (c) Development of toxicity of tetracycline and intermediates

Table 1: Comparison of the photocatalytic performance under visible light irradiation using different photocatalyst

Photocatalyst	Types of Antibiotic s/Pollutants	Amount of catalyst/ Dosage (mg)	Volume (mL), concentration (mg/L)	Efficiency and time	Light Source	Ref.
CoFe ₂ O ₄ @TiO ₂ @rGO	TC and CIP	30	20,10	92% TC; 84% CIP in 90 min	Visible light (500 W Halogen lamp)	[116]
γ -Fe ₂ O ₃ /g-C ₃ N ₄	TC	50	10	73.80% in 120 min	500 W Xe lamp($\lambda > 420 \text{ nm}$)	[117]
ZnO/NiO/g-C ₃ N ₄	TC	50	20	91.49% in 60 min	Visible light (500 W Halogen lamp)	[118]
Fe ₃ O ₄ /BiVO ₄ /CdS	TC	100	10	87.37% in 90 min	300 W Xe lamp	[119]
ZnO-BiWO ₆ /Ti ₃ C ₂ MXene	CIP	50	5	77% in 160 min	Natural light	[120]
Ag ₂ CO ₃ /Bi ₄ O ₅ I ₂ /g-C ₃ N ₄	TC	30	20	82.61% in 30 min	300 W Xe lamp	[121]
NiFe ₂ O ₄ /CeO ₂ /GO	TC	50	20	95% in 90 min	300 W Xe lamp($\lambda = 420 \text{ nm}$)	This work

4. Computational Method

The Vienna Ab initio Simulation Package (VASP) implemented density functional theory (DFT) to calculate the structural and electrical characteristics of CeO₂, NiFe₂O₄, and NiFe₂O₄/CeO₂ [122, 123]. The wave functions are enlarged in plane waves with an energy cutoff of 550 eV using the projector augmented wave technique [124] to characterize the interactions between the valence and core electrons. When there is an energy difference of 10⁻⁶ or less between two successive iterations, the calculations were optimized using the conjugate gradient approach for geometric optimization. The Davidson method is used to minimize the Hellman-Feynman force, which is meant to converge if there is a difference of 0.01 eV/Ång between two successive iterations. This process achieves geometric relaxation. Reducible gamma-centered K-POINTS 10x10x10 are utilized for the bulk computation. The optimized kinetic energy cutoff, k-point, and lattice parameter optimizations were performed using the Perdew–Burke–Ernzerhof (PBE) computations to get precise structural and electrical characteristics [125].

4.1 Structural Optimization

Our computational investigation commenced with the bulk CeO₂ structure, known for its fluorite structure characterized by the Fm3m space group. This configuration features a simple cubic oxygen sublattice, with Ce ions strategically positioned at alternating cube centers. The relaxed state of the structure is depicted in Figure 15 ((A) (a)), where the cerium ion is situated at the core of the tetrahedron, and oxygen atoms (depicted as red spheres) form the vertices. Subsequently, we proceeded to analyze the crystal structure parameters of the compound NiFe₂O₄ (Figure 15 (A) (b)), a spinel ferrite, using the volume optimization technique in the subsequent phase of our investigation. Typically, spinel ferrites are composed of a unit cell that possesses a face-centered cubic (fcc) lattice structure, where the cations are meticulously arranged at sites known as tetrahedral (Th) and octahedral (Oh) positions, referred to as A and B respectively, and are intricately coordinated with oxygen atoms. They are categorized as either normal- or inverse-phase based on how X²⁺ (where X represents Ni, Mg, Co, Zn, Mn) and Fe³⁺ are distributed between the Th and Oh sites. In the normal spinel ferrite structure, the Th sites are occupied by X²⁺ cations, while the Oh sites are populated by Fe³⁺ cations. The inverse phase emerges when the Fe³⁺ cations fully occupy the Oh sites, and the Th sites are haphazardly filled with a combination of Fe³⁺ and Ni²⁺ ions. The extensively researched inverse spinel, nickel ferrite having a space group designation of 227, exhibits a distinctive arrangement. In this structure, Ni atoms are positioned at the 8a tetrahedral sites (1/8, 1/8, 1/8), Fe atoms occupy the 16d octahedral sites (1/2, 1/2, 1/2), and O atoms reside at the 32e face-centered cubic structure sites (u, u, u). Structural optimization has been done for NiFe₂O₄, and as a result, we obtained an optimized value of a₀=8.365 Ång and u=0.27 employing the PBE method, which is in good agreement with the experimental data. Graphitic Oxide (GO) exhibits a structurally unique and less ordered configuration compared to pristine graphite. The absence of a well-defined space group underscores the amorphous nature of graphite oxide, arising from the introduction of oxygen-containing functional groups during the oxidation process. The construction of a 4x4x1 supercell of GO is undertaken to envelop the composite's surface area, yielding a lattice mismatch of 1.9%. The interlayer spacing between composite and GO was determined to be 3.06 Ång, aligning closely with reported values for GO-

based photocatalysts [126, 127]. In the end, we built NiFe₂O₄/CeO₂/GO composite design and structure optimization. The composite structure is designed by using Material Studio and optimized in VASP until reached required accuracy.

4.2 Electronic Properties

CeO₂ exhibits the properties of a wide bandgap semiconductor, possessing a primary energy gap of ~2.42-3.0 eV. The conduction band is shaped by the Ce4f states, whereas the valence band is constituted by the O2p states. The effective mass of the electrons (m_e) is remarkably high as a result of the minimal dispersion exhibited by the f-bands. In contrast to charge transport in conventional semiconductors, where charge carriers can move within their respective bands, the electrons within CeO₂ are highly localized on a Ce atom, giving rise to a small polaron. The density of states (DOS) assists in comprehending how states are distributed within specific energy ranges, offering insights into both unoccupied and occupied states. The states that can be occupied are described by a significant density of states at a particular energy level, but there are no states occupied when the density of states is zero. The density of states for CeO₂ exhibits a discontinuity within the range spanning from the upper limit of the valence band to the lower limit of the conduction band, which typically corresponds to the system's bandgap. The band structures and density of states of CeO₂ computed with the PBE approximation are illustrated in Figure 15 ((B) (a) and (b)), respectively. The density of states shown in Figure 15 ((B) (b)) arises from the incorporation of O2p orbitals (ranging from 5 eV to 9 eV), Ce4f orbitals (ranging from 0.5 eV to 1.7 eV), and Ce5d orbitals (ranging from -1.8 eV to -5 eV). The calculated bandgap of CeO₂ spans from O2p to Ce4f with a width of 3.6 eV, and from O2p to Ce5d with a width of 6.8 eV. The acquired band structure, illustrated in Figure 15 ((C) (a)), unveils the lack of band intersections in the vicinity of the Fermi level. This observation allows us to infer that the calculated band structure of NiFe₂O₄ exhibits semiconductor characteristics, featuring a gap energy of approximately 1.67 eV, which aligns with the results obtained from experimental studies. Figure 15 ((C) (a-b)) shows the total density of states (TDOS) and partial density of states (PDOS) of individual atoms in NiFe₂O₄. The O²⁻ states dominate the valence band, where they also set the band edge. The Ni²⁺ states influence the VB to some extent, below the VB edge, and is determined by an overlap of O²⁻ and Ni²⁺ states. Except for a little contribution from the O²⁻ states, the conduction band edge primarily depends on the Fe³⁺ tetrahedral states. Fe³⁺ octahedral states again dominate the CB, with little contribution from O²⁻ states. Thus, these are the Fe³⁺ tetrahedral and octahedral states that control the CB band edge in the inverse spinel NiFe₂O₄. In the end, the electronic structures of the isolated bulk structure of NiFe₂O₄/CeO₂/GO were calculated, including the band structure and partial density of states (PDOS). An analysis of the electronic band structures of the composite revealed that its conduction band minimum (CBM) and valence band maximum (VBM) are positioned at the same high-symmetry Γ -S locations in the Brillouin zone, making it phases direct bandgap semiconductors. It can be observed from the predicted PDOS that the VBM consists mostly of Ce-5d and Ni-3p atomic orbitals, whereas the CBM principally of Fe-5s, O-3p, and C-2p orbitals. Meanwhile, a considerable hybridization between the Ce-4f state and the GO sheets' C-2p and O-2p states occurred at the CBM. The calculated band gap energy at 1.17 eV in (Figure 15 (D) (a-b)), the correctness and reliability of the theoretical approach and parameters used in this work were confirmed by the nanocomposites' consistency with the experimental results.

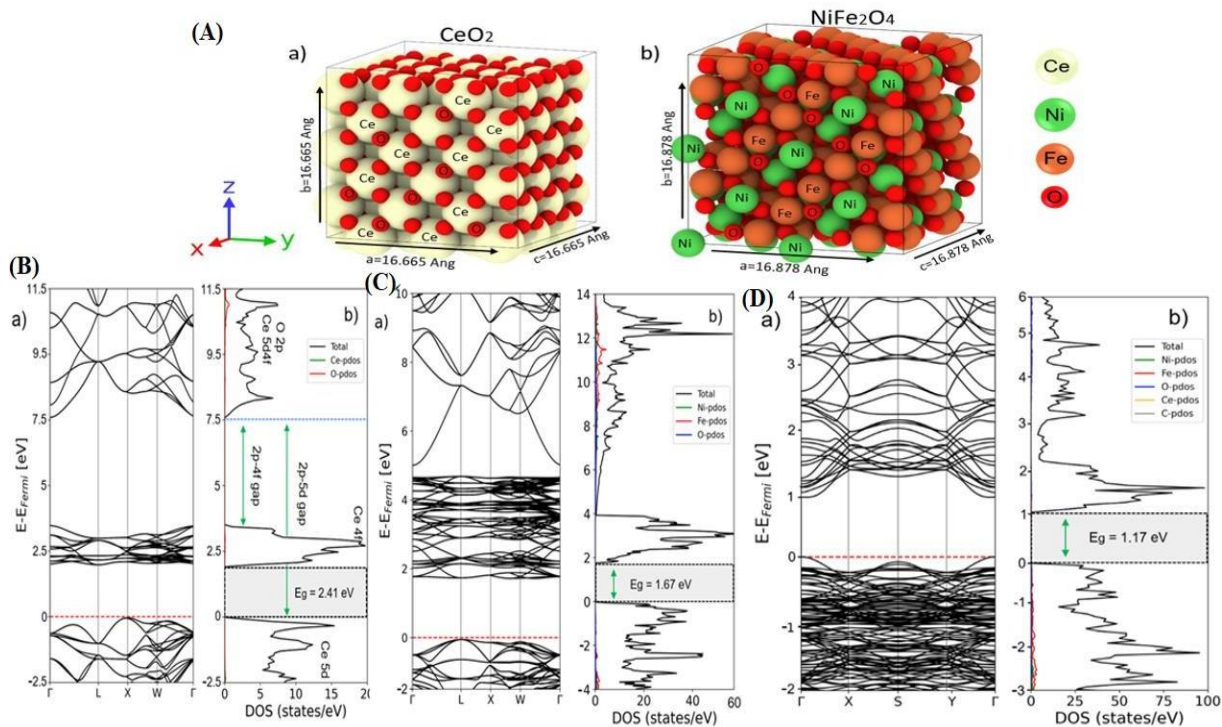


Figure 15 (A): The optimized structure of a) 3x3x3 CeO_2 and b) 2x2x2 NiFe_2O_4 crystals. (B): Band structure and (partial) density of states of CeO_2 . The red line in the band structure plots represents the Fermi energy (C): Band structure and (partial) density of states of NiFe_2O_4 (D): Band structure and (partial) density of states of $\text{NiFe}_2\text{O}_4/\text{CeO}_2/\text{GO}$.

5. Antibacterial activity

The antibacterial activity of $\text{NiFe}_2\text{O}_4/\text{CeO}_2/\text{GO}$ NC was evaluated with varying concentrations including $10 \mu\text{g/mL}$, $20 \mu\text{g/mL}$, $30 \mu\text{g/mL}$, and $40 \mu\text{g/mL}$ against *S. aureus* and *E. coli* which are gram-positive and gram-negative bacterial strains respectively. The antibacterial activity was evaluated using the disc-diffusion method. As demonstrated in Figures 16(a) and 16(c) for *S. aureus* and *E. coli*, respectively, chloramphenicol was used as the positive control as a reference. It is seen that Figures 16(b) and 16(d) for *S. aureus* and *E. coli* show the antibacterial activity of $\text{NiFe}_2\text{O}_4/\text{CeO}_2/\text{GO}$ at concentrations of $10 \mu\text{g/mL}$, $20 \mu\text{g/mL}$, $30 \mu\text{g/mL}$, and $40 \mu\text{g/mL}$, which inhibited the inhibition zones. Furthermore, the antibacterial activity of $\text{NiFe}_2\text{O}_4/\text{CeO}_2/\text{GO}$ NC at different concentrations is compared using a bar graph that illustrates the dose-dependent behavior in Figure 16(e). The amount of inhibition for both bacterial strains increased with the concentration

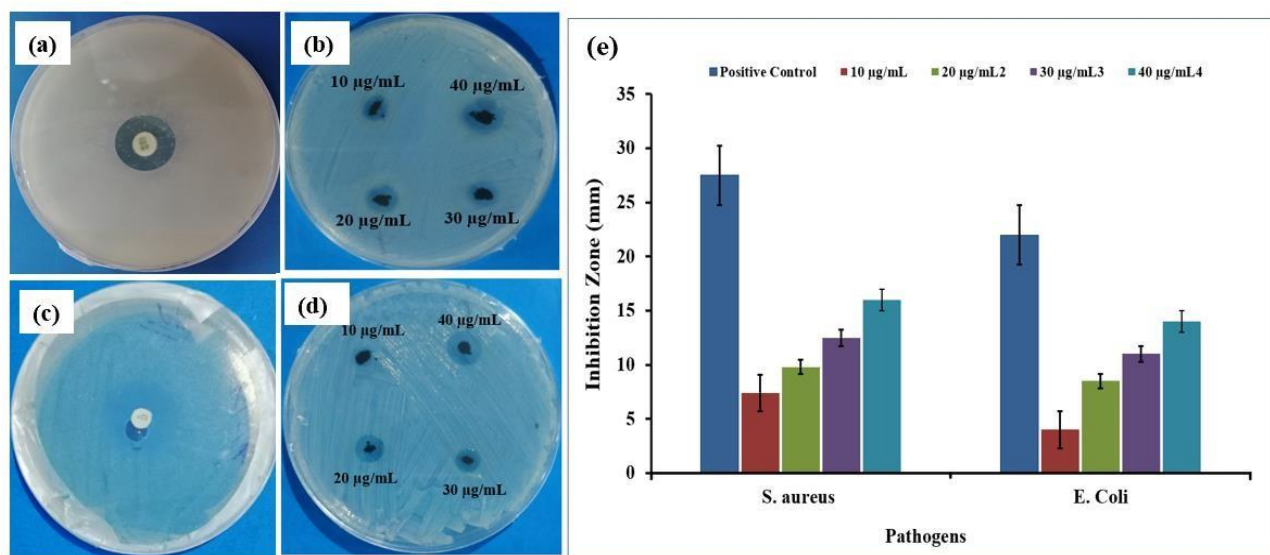


Figure 16: Antibacterial activity of (a) chloramphenicol against *S. aureus* strains (b) NiFe₂O₄/CeO₂/GO with varying concentrations (10-40) µg/mL against *S. aureus* (c) chloramphenicol against *E. coli* (d) NiFe₂O₄/CeO₂/GO with varying concentrations against *E. coli* (e) bar graph for comparison of NiFe₂O₄/CeO₂/GO (10-40) µg/mL against *S. aureus* and *E. coli*

NiFe₂O₄/CeO₂/GO nanocomposite showed a greater inhibition zone against *S. aureus* as compared to *E. coli*. NiFe₂O₄/CeO₂/GO nanocomposite with a concentration of 40 µg/mL showed an inhibition zone of 16 mm and 14 mm against *S. aureus* and *E. coli* respectively. The greater inhibition of nanocomposite against *S. aureus* compared to *E. coli* is due to a complex phenomenon with multiple contributing factors such as Gram-positive bacteria have a simpler cell wall structure, primarily composed of peptidoglycan. The negatively charged peptidoglycan of *S. aureus* attracts positively charged nanoparticles through electrostatic interactions, facilitating adhesion and penetration. Herewith, NiFe₂O₄/CeO₂/GO NC may damage the bacterial cell membrane through various mechanisms like direct contact, ion release, and reactive oxygen species (ROS) generation. ROS disrupts cell integrity and leads to leakage of essential cellular components, ultimately killing the bacteria.

5.1 Molecular Docking Analysis:

The application of computational tools to investigate the underlying mechanisms of biological activities and functions is widely reported [128,129]. Enzymes are widely recognized as the primary contributors to bacterial infection, and hence, suppressing their activity is crucial in combating the resulting infection [129]. The molecular docking analysis of the NiFe₂O₄/CeO₂/GO nanocomposite against the FabI and DNA gyrase enzymes of *E. coli* and *S. aureus* demonstrated that they effectively block these specific enzyme targets. This was indicated by their strong binding affinity within the corresponding binding pockets. The docking analysis of

NiFe₂O₄/CeO₂/GO NC with FabIE. coli demonstrated hydrogen bonding interactions with Thr194, Ile200, Ala197, Tyr156, Lys201, and Tyr146, resulting in a binding score of -7.2 kcal mol⁻¹ (Fig. 17 (A) (a-c)). The NiFe₂O₄/CeO₂/GO NC compound docked against FabIS. aureus showed a binding energy of -6.0 kcal mol⁻¹. The interaction between the complex and the amino acids His247, Asn245, Lys172, Glu168, Ala165, Ala169, Glu151, and Lys172 was observed through hydrogen bonding, as depicted in Fig. 17 (B) (a-c). In addition, the binding potential of NiFe₂O₄/CeO₂/GO NC was evaluated by analyzing the docking predictions for DNA gyrase from E. coli. The binding score was found to be -6.32 kcal mol⁻¹. The evaluation focused on the active sites Ile78, Asn46, Ala47, Thr165, Val71, Asp73, Gly77, Val167, and Val43, as shown in Fig. 17 (C) (a-c).

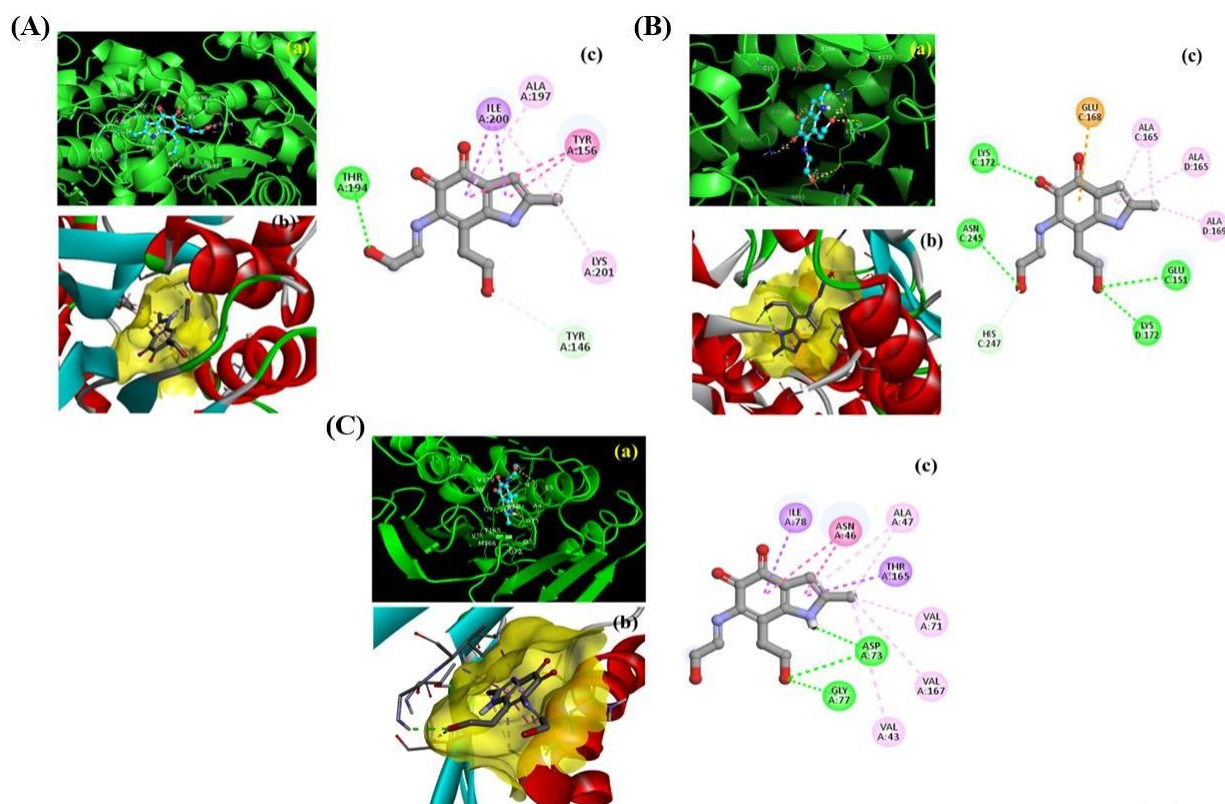


Figure 17: Binding interactions of NiFe₂O₄/CeO₂/GO NC (a-b) (3D), (c) (2D)), inside the active pocket (a) FabIE.coli complex (b) FabIS. aureus complex (c) DNA gyrase from E. coli complex

Conclusion

In this study, NiFe₂O₄/CeO₂/GO nanocomposite photocatalyst was prepared using a hydrothermal approach. The bactericidal activity of the NiFe₂O₄/CeO₂/GO nanocomposite attributed to the inhibition of FabI and DNA gyrase, as revealed through in silico docking investigations. According to the current findings, NiFe₂O₄ and CeO₂ were deposited on GO,

which lowered the amount of photoinduced recombination of charged carriers, promoted charge carrier transport, and enhanced photocatalytic activity. NiFe₂O₄/CeO₂/GO photocatalyst revealed an excellent TC removal with an efficiency of 95% in 90 minutes. Additionally, it was exposed that holes h⁺ and hydroxyl radicals prevailed in the breakdown of TC-HCl, and the NiFe₂O₄/CeO₂/GO photocatalyst persisted in working well even after five cycles. After investigating the degradation intermediates of TC- HCl via LC-MS, the potential pathway in lower molecular intermediates and successive decomposition showed further to create carbon dioxide and water. The findings from the DFT investigation revealed that the contact interfaces between NiFe₂O₄ and CeO₂ in the solid-solid state were established through chemical bonding rather than physical absorption. Adjustments in the CB and VB positions of NiFe₂O₄ and CeO₂ occurred as a result of variations in the Fermi level, leading to the creation of a favorable structure. Overall, the NiFe₂O₄/CeO₂/GO may serve as an excellent photocatalytic candidate nanocomposite for pharmaceutical degradation and may be practiced on a large scale for industrial purposes for water purification and environmental remediation.

Acknowledgment:

This work was supported by the Anhui provincial key research and development plan (Grant no. 202004i07020014). The authors would like to extend their sincere appreciation to the Researcher supporting program at King Saud University, Riyadh, for funding this work under project number (RSP2024R113).

References

- [1] Žur, J., et al., Effects of low concentration of selected analgesics and successive bioaugmentation of the activated sludge on its activity and metabolic diversity. *Water*, 2020. 12(4): p. 1133.
- [2] Bhatia, V., et al., Enhanced photocatalytic degradation of atenolol using graphene TiO₂ composite. *Journal of Photochemistry and Photobiology A: Chemistry*, 2017. 332: p. 182-187.
- [3] Hong, B., et al., Urbanization gradient of selected pharmaceuticals in surface water at a watershed scale. *Science of the Total Environment*, 2018. 634: p. 448-458.
- [4] Daughton, C.G., Cradle-to-cradle stewardship of drugs for minimizing their environmental disposition while promoting human health. I. The rationale for and avenues toward a green pharmacy. *Environmental Health Perspectives*, 2003. 111(5): p. 757-774.
- [5] Choi, Y., et al., Degradation kinetics of antibiotic resistance gene *mecA* of methicillin-resistant *Staphylococcus aureus* (MRSA) during water disinfection with chlorine, ozone, and ultraviolet light. *Environmental Science & Technology*, 2021. 55(4): p. 2541-2552.
- [6] Sun, L., et al., Synergistic effect of single-atom Ag and hierarchical tremella-like g-C₃N₄: electronic structure regulation and multi-channel carriers transport for boosting photocatalytic performance. *Applied Catalysis B: Environmental*, 2022. 306: p. 121106.

- [7] Xiao, C., et al., Carbon-doped defect MoS₂ co-catalytic Fe³⁺/peroxymonosulfate process for efficient sulfadiazine degradation: Accelerating Fe³⁺/Fe²⁺ cycle and 1O₂ dominated oxidation. *Science of The Total Environment*, 2023. 858: p. 159587.
- [8] Minale, M., et al., Application of graphene-based materials for removal of tetracyclines using adsorption and photocatalytic-degradation: A review. *Journal of Environmental Management*, 2020. 276: p. 111310.
- [9] He, X., T. Kai, and P. Ding, Heterojunction photocatalysts for degradation of the tetracycline antibiotic: a review. *Environmental Chemistry Letters*, 2021. 19(6): p. 4563-4601.
- [10] Shi, H., et al., Synthesis of Cu₃P/SnO₂ composites for degradation of tetracycline hydrochloride in wastewater. *RSC advances*, 2021. 11(53): p. 33471-33480.
- [11] Feng, Q., J. Zhou, and Y. Zhang, Coupling Bi₂MoO₆ with persulfate for photocatalytic oxidation of tetracycline hydrochloride under visible light. *Journal of Materials Science: Materials in Electronics*, 2019. 30: p. 19108-19118.
- [12] Yan, T., et al., Construction of 2D/2D Bi₂WO₆/BN heterojunction for effective improvement on photocatalytic degradation of tetracycline. *Journal of Alloys and Compounds*, 2022. 894: p. 162487.
- [13] Foroughi, M., M.H.A. Azqhandi, and S. Kakhki, Bio-inspired, high, and fast adsorption of tetracycline from aqueous media using Fe₃O₄-g-CN@PEI-β-CD nanocomposite: Modeling by response surface methodology (RSM), boosted regression tree (BRT), and general regression neural network (GRNN). *Journal of hazardous materials*, 2020. 388: p. 121769.
- [14] Azqhandi, M.H.A., M. Foroughi, and E. Yazdankish, A highly effective, recyclable, and novel host-guest nanocomposite for Triclosan removal: a comprehensive modeling and optimization-based adsorption study. *Journal of Colloid and interface science*, 2019. 551: p. 195-207.
- [15] Yang, X., et al., Recent advances in photodegradation of antibiotic residues in water. *Chemical Engineering Journal*, 2021. 405: p. 126806.
- [16] Plubphon, N., et al., Rapid preparation of g-C₃N₄/Bi₂O₂CO₃ composites and their enhanced photocatalytic performance. *Diamond and Related Materials*, 2022. 130: p. 109488.
- [17] Zhang, B., et al., Photocatalytic degradation of paracetamol and bisphenol A by chitosan supported covalent organic framework thin film with visible light irradiation. *Journal of Hazardous Materials*, 2022. 435: p. 128966.
- [18] Zhou, T., et al., Tailoring boron doped intramolecular donor–acceptor integrated carbon nitride skeleton with propelling photocatalytic activity and mechanism insight. *Chemical Engineering Journal*, 2022. 445: p. 136643.

- [19] Yan, L., et al., Tremella-like integrated carbon nitride with polyvinylidene-doped for enhancing photocatalytic degradation and hydrogen evolution performances. *Separation and Purification Technology*, 2021. 279: p. 119766.
- [20] Wang, C., et al., Rationally designed tetra (4-carboxyphenyl) porphyrin/graphene quantum dots/bismuth molybdate Z-scheme heterojunction for tetracycline degradation and Cr (VI) reduction: Performance, mechanism, intermediate toxicity appraisalment. *Journal of Colloid and Interface Science*, 2022. 619: p. 307-321.
- [21] Li, S., et al., Designing oxygen vacancy mediated bismuth molybdate (Bi₂MoO₆)/N-rich carbon nitride (C₃N₅) S-scheme heterojunctions for boosted photocatalytic removal of tetracycline antibiotic and Cr (VI): Intermediate toxicity and mechanism insight. *Journal of Colloid and Interface Science*, 2022. 624: p. 219-232.
- [22] Lei, M., et al., Photocatalytic reductive degradation of polybrominated diphenyl ethers on CuO/TiO₂ nanocomposites: a mechanism based on the switching of photocatalytic reduction potential being controlled by the valence state of copper. *Applied Catalysis B: Environmental*, 2016. 182: p. 414-423.
- [23] Sherly, E., J.J. Vijaya, and L.J. Kennedy, Visible-light-induced photocatalytic performances of ZnO–CuO nanocomposites for degradation of 2, 4-dichlorophenol. *Chinese Journal of Catalysis*, 2015. 36(8): p. 1263-1272.
- [24] Vignesh, K., et al., Visible light assisted photocatalytic activity of TiO₂–metal vanadate (M= Sr, Ag and Cd) nanocomposites. *Materials science in semiconductor processing*, 2013. 16(6): p. 1521-1530.
- [25] Xie, L., et al., Morphology engineering of V₂O₅/TiO₂ nanocomposites with enhanced visible light-driven photofunctions for arsenic removal. *Applied Catalysis B: Environmental*, 2016. 184: p. 347-354.
- [26] Yang, W., et al., Enhanced magnetic property and photocatalytic activity of UV-light responsive N-doped Fe₂O₃/FeVO₄ heterojunction. *Ceramics International*, 2015. 41(1): p. 1495-1503.
- [27] Pozan, G.S., M. Isleyen, and S. Gokcen, Transition metal coated TiO₂ nanoparticles: synthesis, characterization and their photocatalytic activity. *Applied Catalysis B: Environmental*, 2013. 140: p. 537-545.
- [28] Liu, X., et al., Microwave-induced catalytic oxidation of malachite green under magnetic Cu-ferrites: new insight into the degradation mechanism and pathway. *Journal of Molecular Catalysis A: Chemical*, 2014. 395: p. 243-250.
- [29] Talebi, R., Preparation of nickel ferrite nanoparticles via a new route and study of their photocatalytic properties. *Journal of Materials Science: Materials in Electronics*, 2017. 28: p. 4058-4063.

- [30] Harish, K., et al., Optical and photocatalytic properties of CdFe₂O₄ nanocatalysts: potential application in water treatment under solar light irradiation. *Archives of Applied Science Research*, 2013. 5(2): p. 42-51.
- [31] Rezsescu, N., et al., Effects of the rare-earth ions on some properties of a nickel-zinc ferrite. *Journal of Physics: Condensed Matter*, 1994. 6(29): p. 5707.
- [32] El Desouky, F.G., et al., Impact of calcination temperature on the structure, optical and photoluminescence properties of Nanocrystalline Cerium oxide thin films. *Materials Science in Semiconductor Processing*, 2020. 111: p. 104991.
- [33] Li, H., et al., Surfactant-assisted synthesis of CeO₂ nanoparticles and their application in wastewater treatment. *RSC Advances*, 2012. 2(32): p. 12413-12423.
- [34] Prabakaran, D.M.D.M., et al., Structural, optical, morphological and dielectric properties of cerium oxide nanoparticles. *Materials Research*, 2016. 19: p. 478-482.
- [35] Liang, Y., et al., TiO₂ nanocrystals grown on graphene as advanced photocatalytic hybrid materials. *Nano Research*, 2010. 3: p. 701-705.
- [36] Williams, G., B. Seger, and P.V. Kamat, TiO₂-graphene nanocomposites. UV-assisted photocatalytic reduction of graphene oxide. *ACS Nano*, 2008. 2(7): p. 1487-1491.
- [37] Liang, J., et al., Scalable green method to fabricate magnetically separable NiFe₂O₄-reduced graphene oxide nanocomposites with enhanced photocatalytic performance driven by visible light. *Industrial & Engineering Chemistry Research*, 2018. 57(12): p. 4311-4319.
- [38] Deng, F., et al., Fabrication of ternary reduced graphene oxide/SnS₂/ZnFe₂O₄ composite for high visible-light photocatalytic activity and stability. *Journal of hazardous materials*, 2017. 332: p. 149-161.
- [39] Zhai, H., et al., Electronic regulation of Pt single-atom catalysts via local coordination state adjustment for enhanced photocatalytic performance. *ACS Catalysis*, 2023. 13(12): p. 8063-8072.
- [40] Zhai, H., et al., Flexible Construction of Heteroatom-free g-C₃N₄/g-C₃N₄ Homojunction with Switching Charge Dynamics Toward Efficient Photo-piezocatalytic Performance. *Applied Catalysis B: Environment and Energy*, 2024: p. 123909.
- [41] Liao, H., et al., Oxyanion engineering suppressed iron segregation in nickel-iron catalysts toward stable water oxidation. *Advanced Materials*, 2023. 35(21): p. 2300347.
- [42] Liu, X., et al., Cationic oxidative leaching engineering modulated in situ self-reconstruction of nickel sulfide for superior water oxidation. *Nano Letters*, 2023. 23(11): p. 5027-5034.

[43] Tong, J., et al., Visible light-driven silver-modified titanium dioxide/bismuth molybdenum oxide with rapid interfacial charge-transfer for dual highly efficient photocatalytic degradation and disinfection. *Journal of Colloid and Interface Science*, 2024. 653: p. 285-295.

[44] Li, S., et al., Ta₃N₅/CdS core-shell S-scheme heterojunction nanofibers for efficient photocatalytic removal of antibiotic tetracycline and Cr (VI): performance and mechanism insights. *Advanced Fiber Materials*, 2023. 5(3): p. 994-1007.

[45] Li, S., et al., A plasmonic S-scheme Au/MIL-101 (Fe)/BiOBr photocatalyst for efficient synchronous decontamination of Cr (VI) and norfloxacin antibiotic. *EScience*, 2024. 4(2): p. 100208.

[46] Li, S., et al., Chemically bonded Mn_{0.5}Cd_{0.5}S/BiOBr S-scheme photocatalyst with rich oxygen vacancies for improved photocatalytic decontamination performance. *Advanced Powder Materials*, 2024: p. 100183.

[47] Wang, C., et al., Carbon quantum dots-modified tetra (4-carboxyphenyl) porphyrin/BiOBr S-scheme heterojunction for efficient photocatalytic antibiotic degradation. *Science China Materials*, 2024: p. 1-11.

[48] Babu, C.M., et al., Characterization of reduced graphene oxide supported mesoporous Fe₂O₃/TiO₂ nanoparticles and adsorption of As (III) and As (V) from potable water. *Journal of the Taiwan Institute of Chemical Engineers*, 2016. 62: p. 199-208.

[49] McKinney, D.C., et al., Antibacterial FabH inhibitors with mode of action validated in *Haemophilus influenzae* by in vitro resistance mutation mapping. *ACS infectious diseases*, 2016. 2(7): p. 456-464.

[50] Ikram, M., et al., Photocatalytic and bactericidal properties and molecular docking analysis of TiO₂ nanoparticles conjugated with Zr for environmental remediation. *RSC advances*, 2020. 10(50): p. 30007-30024.

[51] Panchaud, P., et al., Discovery and optimization of isoquinoline ethyl ureas as antibacterial agents. *Journal of medicinal chemistry*, 2017. 60(9): p. 3755-3775.

[52] Seefeld, M.A., et al., Indole naphthyridinones as inhibitors of bacterial enoyl-ACP reductases FabI and FabK. *Journal of medicinal chemistry*, 2003. 46(9): p. 1627-1635.

[53] Fage, C.D., et al., The Kalimantanacin Polyketide Antibiotics Inhibit Fatty Acid Biosynthesis in *Staphylococcus aureus* by Targeting the Enoyl-Acyl Carrier Protein Binding Site of FabI. *Angewandte Chemie International Edition*, 2020. 59(26): p. 10549-10556.

[54] Baroroh, U., et al., Molecular interaction analysis and visualization of protein-ligand docking using Biovia Discovery Studio Visualizer. *Indonesian Journal of Computational Biology (IJCB)*, 2023. 2(1): p. 22-30.

[55] Umar, E., et al., Improved catalytic and bactericidal behavior with in silico molecular docking analysis of barium/chitosan doped tungstate oxide nanoplates. *Surfaces and Interfaces*, 2023. 38: p. 102835.

[56] Umar, E., et al., In-vitro synergistic microbicidal and catalytic evaluation of polyvinylpyrrolidone/chitosan doped tungsten trioxide nanoplates with evidential in-silico analysis. *International Journal of Biological Macromolecules*, 2023. 242: p. 124815.

[57] Dhiman, M., et al., Designing different NiFe₂O₄ morphologies for tuning structural, optical, and magnetic properties for catalytic advancements. *New Journal of Chemistry*, 2016. 40(12): p. 10418-10431.

[58] Renuka, N.K., Structural characteristics of quantum-size ceria nanoparticles synthesized via simple ammonia precipitation. *Journal of Alloys and Compounds*, 2012. 513: p. 230-235.

[59] Sudharani, A., et al., Solvothermal Synthesis of Coo/Bioi Flower Like Nanocomposites and Efficient Photocatalytic Activity Under Visible-Light. *Bioi Flower Like Nanocomposites and Efficient Photocatalytic Activity Under Visible-Light*.

[60] He, Z., et al., Optimal co-catalytic effect of NiFe₂O₄/ZnO nanocomposites toward enhanced photodegradation for dye MB. *Zeitschrift für Physikalische Chemie*, 2019. 233(3): p. 347-359.

[61] Thema, F., et al., Synthesis and characterization of graphene thin films by chemical reduction of exfoliated and intercalated graphite oxide. *Journal of Chemistry*, 2013. 2013.

[62] Xu, Y., Q. Wang, Y. Cao, X. Wei and B. Huang (2017). "Preparation of a reduced graphene oxide/SiO₂/Fe₃O₄ UV-curing material and its excellent microwave absorption properties." *RSC Advances* 7(29): p. 18172-18177.

[63] Jiang, J., et al., Facile fabrication and characterization of NiFe₂O₄/ZnO hybrid nanoparticles. *Journal of alloys and compounds*, 2009. 484(1-2): p. 69-72.

[64] Sundari, R., et al., The characterization study of ferrites (magnesium and manganese) using sol-gel method. *The Malaysian Journal of Analytical Sciences*, 2014. 18(3): p. 485-490.

[65] Sertkol, M., et al., Microwave synthesis and characterization of Zn-doped nickel ferrite nanoparticles. *Journal of Alloys and Compounds*, 2009. 486(1-2): p. 325-329.

[66] Fu, Y., H. Chen, X. Sun and X. Wang (2012). "Graphene-supported nickel ferrite: A magnetically separable photocatalyst with high activity under visible light." *AIChE Journal* 58(11): p. 3298-3305.

[67] Mo, Z., et al., Preparation and characterization of a PMMA/Ce (OH)₃, Pr₂O₃/graphite nanosheet composite. *Polymer*, 2005. 46(26): p. 12670-12676.

- [68] Zhu, C., et al., Reducing sugar: new functional molecules for the green synthesis of graphene nanosheets. *ACS nano*, 2010. 4(4): p. 2429-2437.
- [69] Baraliya, J. and H. Joshi, Spectroscopy investigation of nanometric cobalt ferrite synthesized by different techniques. *Vibrational Spectroscopy*, 2014. 74: p. 75-80.
- [70] Choi, Y., et al., Characterization of O₂-CeO₂ interactions using in situ Raman spectroscopy and first-principle calculations. *ChemPhysChem*, 2006. 7(9): p. 1957-1963.
- [71] Wu, J.-B., et al., Raman spectroscopy of graphene-based materials and its applications in related devices. *Chemical Society Reviews*, 2018. 47(5): p. 1822-1873.
- [72] Malard, L.M., et al., Raman spectroscopy in graphene. *Physics Reports*, 2009. 473(5-6): p. 51-87.
- [73] Pandey, G. and S. Dixit, Growth mechanism and optical properties determination of CdS nanostructures. *The Journal of Physical Chemistry C*, 2011. 115(36): p. 17633-17642.
- [74] Ciocarlan, R.-G., et al., Novel magnetic nanocomposites containing quaternary ferrites systems Co_{0.5}Zn_{0.25}M_{0.25}Fe₂O₄ (M= Ni, Cu, Mn, Mg) and TiO₂-anatase phase as photocatalysts for wastewater remediation under solar light irradiation. *Materials Science and Engineering: B*, 2018. 230: p. 1-7.
- [75] Akhavan, O., et al., Zinc ferrite spinel-graphene in magneto-photothermal therapy of cancer. *Journal of Materials Chemistry B*, 2014. 2(21): p. 3306-3314.
- [76] Kumar, P.S., et al., CdO nanospheres: facile synthesis and bandgap modification for the superior photocatalytic activity. *Materials Letters*, 2015. 151: p. 45-48.
- [77] Wang, W.-W. and J.-L. Yao, Synthesis of magnetically separable Sn doped magnetite/silica core-shell structure and photocatalytic property. *Materials Research Bulletin*, 2010. 45(6): p. 710-716.
- [78] Sivakumar, P., et al., Synthesis and characterization of NiFe₂O₄ nanosheet via polymer assisted co-precipitation method. *Materials Letters*, 2011. 65(3): p. 483-485.
- [79] Verma, K.C., et al., Structural, microstructural and magnetic properties of NiFe₂O₄, CoFe₂O₄ and MnFe₂O₄ nanoferrite thin films. *Journal of Magnetism and Magnetic Materials*, 2011. 323(24): p. 3271-3275.
- [80] Wang, et al., Monodispersed core-shell Fe₃O₄@Au nanoparticles. *The Journal of Physical Chemistry B*, 2005. 109(46): p. 21593-21601.
- [81] Sangwichien, C., G. Aranovich, and M. Donohue, Density functional theory predictions of adsorption isotherms with hysteresis loops. *Colloids and Surfaces A: Physicochemical and Engineering Aspects*, 2002. 206(1-3): p. 313-320.

- [82] Sing, K.S. and R.T. Williams, Physisorption hysteresis loops and the characterization of nanoporous materials. *Adsorption Science & Technology*, 2004. 22(10): p. 773-782.
- [83] Noor, F., et al., Architecture of GO/CoFe₂O₄/ZnO nanocomposite for efficient fluoride removal: An approach using RSM, ANN and GRU modeling. *Surfaces and Interfaces*, 2023. 43: p. 103583.
- [84] Cai, M., et al., Floatable S-scheme Bi₂WO₆/C₃N₄/carbon fiber cloth composite photocatalyst for efficient water decontamination. *Chinese Journal of Catalysis*, 2023. 52: p. 239-251.
- [85] 王春春, et al., 富含氧空位 S 型 MIL-101 (Fe)/BiOCl 异质结增强光催化去除 Cr (VI). *物理化学学报*, 2023. 40(7): p. 2307045.
- [86] Alna'washi, G., et al., Investigation on X-ray photoelectron spectroscopy, structural and low temperature magnetic properties of Ni-Ti co-substituted M-type strontium hexaferrites prepared by ball milling technique. *Results in Physics*, 2021. 28: p. 104574.
- [87] Pei, Y., et al., Heteroatom-modulated NiCo₂O₄ apparent energy activation of PMS for tetracycline removal: Mechanism and toxicity analysis. *Environmental Research*, 2024. 240: p. 117571.
- [88] Kumaresan, L., et al., Spherically Structured Ce-Metal-Organic Frameworks with Rough Surfaces and Carbon-Coated Cerium Oxide as Potential Electrodes for Lithium Storage and Supercapacitors. *ChemistrySelect*, 2023. 8(10): p. e202204759.
- [89] Alna'washi, G., et al., Magnetic study of M-type Co-Ti doped strontium hexaferrite nanocrystalline particles. *Journal of Superconductivity and Novel Magnetism*, 2020. 33: p. 1423-1432.
- [90] Šimša, Z., et al., Magneto-optical properties of vacancy-defective Mn-ferrite films. *Journal of Magnetism and Magnetic Materials*, 1999. 196: p. 620-621.
- [91] Teng, W., et al., Novel Ag₃PO₄/MoO₃ pn heterojunction with enhanced photocatalytic activity and stability under visible light irradiation. *Applied Surface Science*, 2017. 409: p. 250-260.
- [92] Xie, L., et al., A novel CeO₂-TiO₂/PANI/NiFe₂O₄ magnetic photocatalyst: Preparation, characterization and photodegradation of tetracycline hydrochloride under visible light. *Journal of Solid State Chemistry*, 2021. 300: p. 122208.
- [93] Xie, L., et al., A novel CeO₂-TiO₂/PANI/NiFe₂O₄ magnetic photocatalyst: Preparation, characterization and photodegradation of tetracycline hydrochloride under visible light. *Journal of Solid State Chemistry*, 2021. 300: p. 122208.

- [94] Sreeram, N., et al., Fabrication of InVO₄/SnWO₄ heterostructured photocatalyst for efficient photocatalytic degradation of tetracycline under visible light. *Environmental Research*, 2023. 220: p. 115191.
- [95] Zhang, J., et al., Fabrication of visible-light-driven Bi₂O₃-Bi₃TaO₇ nanocomposite for tetracycline degradation with enhanced photocatalytic efficiency. *Journal of Solid State Chemistry*, 2019. 278: p. 120894.
- [96] Tian, Y., et al., MoS₂ as highly efficient co-catalyst enhancing the performance of Fe⁰ based electro-Fenton process in degradation of sulfamethazine: Approach and mechanism. *Chemical Engineering Journal*, 2021. 403: p. 126361.
- [97] Wang, T., et al., Peroxymonosulfate oxidation of carbamazepine by Iron-Biochar via nonradical pathways: Singlet oxygen, electron transfer, and Fe (IV). *Separation and Purification Technology*, 2024. 328: p. 125134.
- [98] Wang, T., et al., Insight into the synergy between rice shell biochar particle electrodes and peroxymonosulfate in a three-dimensional electrochemical reactor for norfloxacin degradation. *Separation and Purification Technology*, 2023. 304: p. 122354.
- [99] Li, S. and J. Hu, Photolytic and photocatalytic degradation of tetracycline: Effect of humic acid on degradation kinetics and mechanisms. *Journal of Hazardous Materials*, 2016. 318: p. 134-144.
- [100] Xue, Y., et al., Efficient degradation of atrazine by BiOBr/UiO-66 composite photocatalyst under visible light irradiation: Environmental factors, mechanisms and degradation pathways. *Chemosphere*, 2018. 203: p. 497-505.
- [101] Jiang, L., et al., Metal-free efficient photocatalyst for stable visible-light photocatalytic degradation of refractory pollutant. *Applied Catalysis B: Environmental*, 2018. 221: p. 715-725.
- [102] Guo, S., et al., Structure-controlled three-dimensional BiOI/MoS₂ microspheres for boosting visible-light photocatalytic degradation of tetracycline. *Journal of Alloys and Compounds*, 2021. 852: p. 157026.
- [103] Wang, B., et al., Band gap engineering in BiNbO₄ for visible-light photocatalysis. *Applied Physics Letters*, 2012. 100(18): p. 182102.
- [104] Yuan, Q., et al., Cu₂O/BiVO₄ heterostructures: synthesis and application in simultaneous photocatalytic oxidation of organic dyes and reduction of Cr (VI) under visible light. *Chemical Engineering Journal*, 2014. 255: p. 394-404.
- [105] Li, S., et al., BiO⁺COOH microflowers decorated with Ag/Ag₂CrO₄ nanoparticles as highly efficient photocatalyst for the treatment of toxic wastewater. *Catalysts*, 2020. 10(1): p. 93.

- [106] Ren, L., et al., Defects-engineering of magnetic γ -Fe₂O₃ ultrathin nanosheets/mesoporous black TiO₂ hollow sphere heterojunctions for efficient charge separation and the solar-driven photocatalytic mechanism of tetracycline degradation. *Applied Catalysis B: Environmental*, 2019. 240: p. 319-328.
- [107] Li, H., et al., Enhanced activation of molecular oxygen and degradation of tetracycline over Cu-S₄ atomic clusters. *Applied Catalysis B: Environmental*, 2020. 272: p. 118966.
- [108] Wang, H., et al., Enhanced visible-light photocatalytic degradation of tetracycline by a novel hollow BiOCl@CeO₂ heterostructured microspheres: Structural characterization and reaction mechanism. *Journal of hazardous materials*, 2020. 385: p. 121552.
- [109] Ye, Z., et al., Well-dispersed nebula-like ZnO/CeO₂@HNTs heterostructure for efficient photocatalytic degradation of tetracycline. *Chemical Engineering Journal*, 2016. 304: p. 917-933.
- [110] Li, S., et al., Photocatalytic degradation of antibiotics using a novel Ag/Ag₂S/Bi₂MoO₆ plasmonic pn heterojunction photocatalyst: Mineralization activity, degradation pathways and boosted charge separation mechanism. *Chemical Engineering Journal*, 2021. 415: p. 128991.
- [111] Wang, J., et al., The generation of lattice oxygen defects enhanced by β particles: Layered microsphere-like Bi₂WO₆ as a template leads to Bi_x@Bi_{2-x}WO_n for the efficient removal of oxytetracycline. *Chemical Engineering Journal*, 2021. 416: p. 129197.
- [112] Zhou, B., et al., Controlled synthesis of rh-In₂O₃ nanostructures with different morphologies for efficient photocatalytic degradation of oxytetracycline. *Applied Surface Science*, 2019. 464: p. 115-124.
- [113] Guo, F., et al., Prominent co-catalytic effect of CoP nanoparticles anchored on high-crystalline g-C₃N₄ nanosheets for enhanced visible-light photocatalytic degradation of tetracycline in wastewater. *Chemical Engineering Journal*, 2020. 395: p. 125118.
- [114] Yi, X.-H., et al., Photocatalysis-activated SR-AOP over PDINH/MIL-88A (Fe) composites for boosted chloroquine phosphate degradation: Performance, mechanism, pathway and DFT calculations. *Applied Catalysis B: Environmental*, 2021. 293: p. 120229.
- [115] Wang, F.-X., et al., Efficient removal of emerging organic contaminants via photo-Fenton process over micron-sized Fe-MOF sheet. *Chemical Engineering Journal*, 2022. 429: p. 132495.
- [116] Nimshi, R. E., J. J. Vijaya, L. J. Kennedy, P. S. Selvamani, M. Bououdina and P. J. Sophia (2023). "Effective microwave assisted synthesis of CoFe₂O₄@TiO₂@rGO ternary nanocomposites for the synergic sonophotocatalytic degradation of tetracycline and c antibiotics." *Ceramics International* 49(9): p. 13762-13773.
- [117] C. Li, S. Yu, H. Che, X. Zhang, J. Han, Y. Mao, Y. Wang, C. Liu, H. Dong, Fabrication of Z-Scheme heterojunction by anchoring mesoporous γ -Fe₂O₃ nanospheres on g-C₃N₄ for

degrading tetracycline hydrochloride in water, *ACS Sustain. Chem. Eng.* 6 (2018) p. 16437–16447.

[118] N. Dineshbabu, R.N. Jayaprakash, P. Karuppasamy, T. Arun, J.J. Vijaya, R. E. Nimshi, M.S. Pandian, S.M. Packiam, P. Ramasamy, Investigation on Tetracycline degradation and bactericidal properties of binary and ternary ZnO/NiO/g-C₃N₄ composites prepared by a facile co-precipitation method, *J. Environ. Chem. Eng.* 10 (2022), p. 107368.

[119] G. Xu, M. Du, T. Li, Y. Guan, C. Guo, Facile synthesis of magnetically retrievable Fe₃O₄/BiVO₄/CdS heterojunction composite for enhanced photocatalytic degradation of tetracycline under visible light, *Sep. Purif. Technol.* 275 (2021), p. 119157.

[120] V. Sharma, A. Kumar, A. Kumar, V. Krishnan, Enhanced photocatalytic activity of two-dimensional ternary nanocomposites of ZnO–Bi₂WO₆–Ti₃C₂ MXene under natural sunlight irradiation, *Chemosphere* 287 (2022), p. 132119.

[121] Z.J. Chen, H. Guo, H.Y. Liu, C.G. Niu, D.W. Huang, Y.Y. Yang, C. Liang, L. Li, J. C. Li, Construction of dual S-scheme Ag₂CO₃/Bi₄O₅I₂/g-C₃N₄ heterostructure photocatalyst with enhanced visible-light photocatalytic degradation for tetracycline, *Chem. Eng. J.* 438 (2022), p. 135471.

[122] Hasan, N., et al., Magnetic, optoelectronic, and rietveld refined structural properties of Al³⁺ substituted nanocrystalline Ni-Cu spinel ferrites: An experimental and DFT based study. *Journal of Magnetism and Magnetic Materials*, 2023, 573, p. 170675.

[123] Hou, Y., et al., Structural, electronic and magnetic properties of manganese substituted CoFe₂O₄: a first-principles study. *Journal of Magnetism and Magnetic Materials*, 2020, 495, p. 165862.

[124] Bindra, J., et al., Evidence of ferrimagnetism in Fe-doped CdSe quantum dots. *Chemistry of Materials*, 2018, 30(23), p. 8446-8456.

[125] Jiang, H., et al., Design, preparation, characterization, and application of Mn_xCu_{1-x}O_y/γ-Al₂O₃ catalysts in ozonation to achieve simultaneous organic carbon and nitrogen removal in pyridine wastewater. *Science of The Total Environment*, 2021, 774, p. 145189.

[126] Opoku, F., Govender, K. K., van Sittert, C. G. C. E., & Govender, P. P. (2018). Tuning the electronic structures, work functions, optical properties and stability of bifunctional hybrid graphene oxide/V-doped NaNbO₃ type-II heterostructures: A promising photocatalyst for H₂ production. *Carbon*, 136, p. 187-195.

[127] Opong, S. O. B., Opoku, F., Anku, W. W., Kiarri, E. M., & Govender, P. P. (2019). Experimental and computational design of highly active Ce–ZrO₂–GO photocatalyst for eosin yellow dye degradation: the role of interface and Ce³⁺ ion. *Catalysis Letters*, 149, p. 1633-1650.

[128] Arularasu, M., M. Harb, and R. Sundaram, Synthesis and characterization of cellulose/TiO₂ nanocomposite: Evaluation of in vitro antibacterial and in silico molecular docking studies. Carbohydrate polymers, 2020. 249: p. 116868.

[129] Ikram, M., et al., Dye degradation performance, bactericidal behavior and molecular docking analysis of Cu-doped TiO₂ nanoparticles. RSC advances, 2020. 10(41): p. 24215-24233.